



**Politecnico
di Torino**

Politecnico di Torino

Corso di Laurea Magistrale in Ingegneria Meccanica

A.a. 2023/2024

Sessione di Laurea ottobre 2024

NVH analysis for Rotary Regenerative Shock Absorber

Relatori:

Prof. AMATI NICOLA

Dr. SORRENTINO GENNARO

Dr. BISCIAIO GIORGIO

Candidati:

ROSMARINO GABRIELE

MAT. 286309

*A mia sorella Caterina,
manchi dannatamente.*

Acknowledgment

This thesis work has been developed in the “Centre for Automotive Research and Sustainable mobility” (C.A.R.S) at Politecnico of Turin.

Firstly, I want to thank the professor Amati for accepting me as a thesis student and in this way giving me the opportunity to deal with a challenging and never boring environment: the automotive one. I want to thank him for giving me some interesting food for thought and feedback.

I am very thankful to Gennaro and Giorgio. Their advice, support and friendship have been of vital importance. They were always available whenever I needed them and for that I am incredibly grateful. This allows me to face this experience in a friendly environment. I also want to thank all the other guys who made me spend all these months with a smile and the right mood.

I want to thank my family: mum, dad, and grandma. We have faced some difficult moments, but you never put pressure on me. This made a substantial difference because in this way I always felt your support. I hope to repay all your efforts as soon as possible.

The greatest thank goes to my love Delia. She has always been there without ever having to ask, despite the distance. She is the most important person in my life, now and forever.

Finally, a great thank goes to my friend: Antonino, Claudio, Fabio M., Fabio S. They fulfilled my life with joy and little moments that will remain etched in my life.

Abstract

In recent decades, increasing attention has been directed towards improving comfort and driving stability. In this context, the demand for suspension systems capable of effectively adapting to the excitations coming from the road irregularities became evident. This led to the development of semi-active and active suspensions, now available even in non-premium vehicles. In addition, the need to reduce CO₂ emissions, and thus become sustainable for the planet, has led the automotive industry to considerable changes. In recent years, there has been a further push in the electrification direction. This is remarked by the development of systems, which enhance the efficiency of the electric vehicle through energy harvesting. A glaring example is the *Rotary Regenerative Shock Absorber (RRSA)*, which is the focus of this thesis. It is an electromagnetic damper composed of a Surface Permanent Magnet (SPM) motor, a gearbox and a leverage system linked with the vehicle suspension, which allows a linear-to-rotary motion conversion. Of course, electrification has impacted all parts of the vehicle, but primarily the powertrain. The adoption of electric motors, replacing internal combustion engines (ICE), has changed the background noise inside the vehicle cabin, eliminating the main source of acoustic discomfort felt by passengers. Electric engines in fact produce a typical tonal noise in the high frequency range, which has less impact on human body. As a result, it has become of vital importance to conduct Noise, Vibration and Harshness (NVH) analysis not only for the powertrain but also for all other devices, such as the suspension system. All these new components for the active control purpose could lead to a potential increase of the generated noises. NVH analysis has become increasingly popular as “vehicle sound quality” now plays a crucial role in the consumers’ vehicle choice.

The main aim of this thesis is to carry out a NVH analysis of the RRSA in two different contexts: experimental and simulative environment. For the experimental campaign, a comparison is made between two different prototypes. Both share the same electric motor but differ for the speed reducer they exploit: the starting version is equipped with a planetary gearbox; the new prototype is equipped with a cycloidal gearbox instead. In parallel, a simulation analysis has been conducted. The aim is to investigate further the planetary solution, to get an order analysis of the system, and identify the main noise sources. Also, it is useful to develop a digital twin of the prototype and validate it comparing the results with experimental data in order to have a starting point for simulating next developments, i.e. planetary gearbox equipped with helicoidal gears.

Contents

1 PREFACE.....	1
1.1 Suspension systems overview.....	1
1.1.1 Semi active suspension systems	3
1.1.2 Active suspension systems.....	4
1.1.3 Rotary regenerative shock absorber	6
1.2 NVH analysis methods for automotive applications.....	9
1.2.1 Structure-borne and airborne path NVH	10
1.2.2 Noise sources in a passenger car	11
1.2.3 Experimental method in automotive environment: Transfer Path Analysis	15
1.3 Noise and vibration sources in RRSA.....	17
1.3.1 Geartrain NVH.....	17
1.3.2 Electric motor NVH	18
1.4 Thesis outline	19
2 EXPERIMENTAL ANALYSIS: PLANETARY VS CYCLOIDAL RRSA	20
2.1 Test bench configuration.....	22
2.1.1 Test bench Impact Testing.....	25
2.2 Test procedure.....	27
2.3 Test results	28
2.3.1 Planetary prototype results	28
2.3.1.1 Planetary vibration analysis.....	30
2.3.1.2 Planetary acoustic analysis.....	34
2.3.2 Cycloidal prototype results	40
2.3.2.1 Cycloidal vibrational analysis.....	40
2.3.2.2 Cycloidal acoustic analysis.....	43
2.3.3 Results overview and prototypes comparison.....	48
2.3.3.1 Active vs Regenerative mode	49
2.3.3.2 Planetary vs Cycloidal Prototype	50
3 SIMULATION ANALYSIS	54
3.1 Simulation methodologies in automotive industry	54
3.1.1 Finite element method (FEM).....	54
3.1.2 Boundary element method (BEM).....	55
3.1.3 Infinite element method (IEM)	55
3.1.4 Statistical energy analysis (SEA)	56
3.2 Simulation environment	56

3.2.1	AVL® Excite M	56
3.2.2	RRSA Planetary prototype in Excite M	58
3.2.3	Simulation method used in AVL® software	59
3.3	Simulation results.....	60
	CONCLUSIONS.....	65
	BIBLIOGRAPHY.....	67

1 Preface

1.1 Suspension systems overview

Nowadays one of the main aims in the automotive industry is to limit CO₂ emissions. New and increasingly strict regulations are spreading worldwide. For this purpose, electric vehicles (EV) are widely used [1]. Over the years, in addition to the increasing popularity of electric vehicles, more and more electric devices have been integrated into the passenger compartment. These technologies aim to substitute the mechanical and hydraulic connections with electrical components. Indeed “X-by-wire” technologies are becoming increasingly competitive with respect to the mechanical ones. The main advantages are their higher performance and smaller sensitivity respect to the working environment and finally the energy saving that they can allow thanks to weight reduction and regenerative capability [2]. Obviously, in addition to the advantages, there are also some drawbacks, such as increased complexity and dependence from electronics.

In the last decades, to take an important step towards the electrification of the powertrain and chassis, in addition to the better known ‘X-by-wire’ technologies, such as ‘steer-by-wire’ or ‘brake-by-wire’, work has begun on ‘suspensions-by-wire’ technologies.

The suspension system is a device that decouple the sprung mass with respect to the tyre in order to limit the vibrations that come from the road irregularities. Today’s cars are mostly equipped with passive suspension systems because of their simplicity and cheapness. These, usually, consist of a gas or coil spring in parallel with a hydraulic piston.

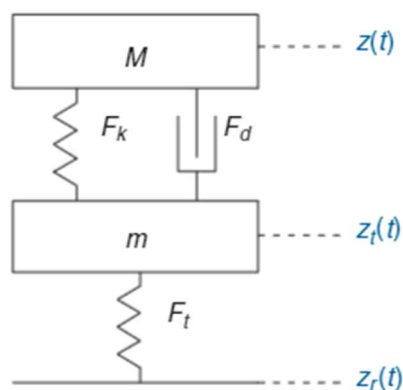


Figure 1 – Passive suspension quarter-car model [3]

On the other hand, the electronically controlled suspension systems can be classified with respect to the energy input and the bandwidth of the actuator [3].

This classification leads to five main categories of controllable suspensions:

- *Adaptive suspension*: the control action is represented by a slow modulation of damping. The shock absorber is characterized by a bandwidth of a few Hertz.
- *Semi-active suspension*: it presents an electronic shock absorber able to change the damping with a large bandwidth (around 30-40 Hz).
- *Load-leveling suspensions*: these are capable of introduce energy into the system (active suspension) to change the steady state condition.
- *Slow-active suspensions*: an actuator replace the passive device of the suspension, and it gives a force F that is the controlled input. The bandwidth is limited to a few Hertz.
- *Fully active suspensions*: these differ from the slow-active suspension only by the bandwidth (30-40 Hz).

System class	Control range (spring)	Control range (damper)	Control bandwidth	Power request	Control variable
Passive			-	-	-
Adaptive			1-5 Hz	10-20 W	c (damping ratio)
Semi-active			30-40 Hz	10-20 W	c (damping ratio)
Load leveling			0.1-1 Hz	100-200 W	W (static load)
Slow active			1-5 Hz	1-5 kW	F (force)
Fully active			20-30 Hz	5-10 kW	F (force)

Figure 2 – Classification of electronically controlled suspension [3]

1.1.1 Semi active suspension systems

Since 1980s, the introduction of semi-active suspension systems has been very promising and obtained very good results in reducing the vibration of sprung mass. As previous stated, a semi active suspension system has a shock absorber able to vary the damping ratio with an associated bandwidth of 20-30 Hz. Nowadays the most common technologies used to achieve these performances are:

- *Electrohydraulic Dampers (EH Dampers)*: unlike the classical passive element, they have electronic valves instead of classic ones.
- *Magnetorheological Dampers (MR Dampers)*: these exploit the physical properties of magnetorheological fluids, which are changing their viscosity when crossed by a magnetic field.
- *Electrorheological Dampers (ER Dampers)*: as magnetorheological ones but they are filled with electrorheological fluids, which vary their viscosity when crossed by an electric field.

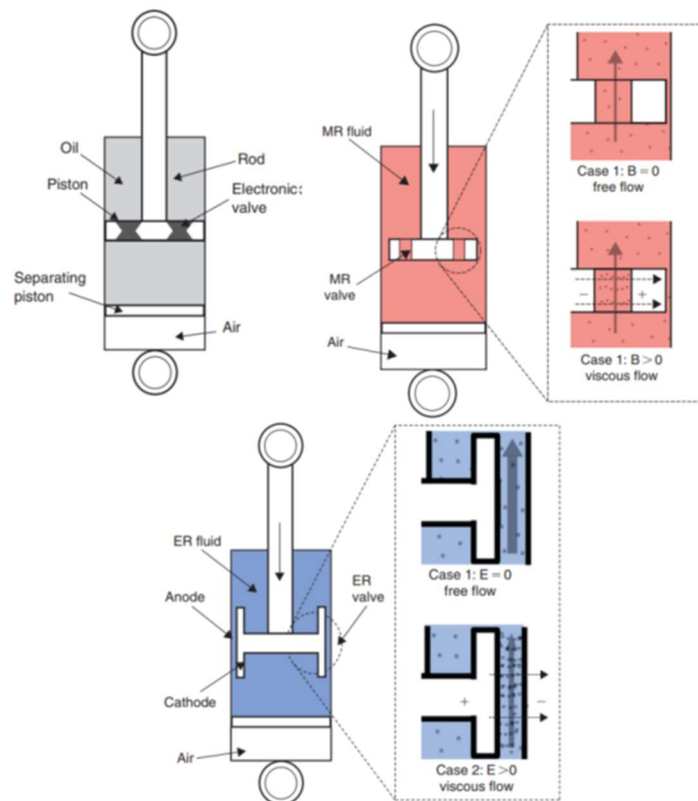


Figure 3 – Schematic representation of EM (top left), MR (top right) and ER (bottom centre) semi-active dampers [3]

1.1.2 Active suspension systems

The ultimate expression of suspension systems are the active ones. Already in the last century, active suspension systems were becoming increasingly popular. But since around 2010, as the demand for electric vehicles has grown, the search for new active suspension systems has increased. In fact, the automotive suspension system market is expected to grow from 4.53×10^{10} USD in 2022 to 5.16×10^{10} USD in 2027 [4]. Similarly, academic studies on active suspension systems have also seen enormous growth, as shown in the figure below.

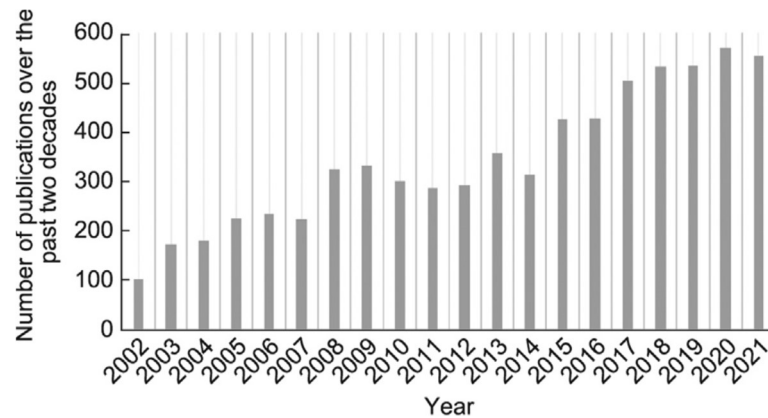


Figure 4 - Number of publications about active suspension systems in the last decades [4]

The active suspension systems are cutting-edge technologies designed to enhance vehicle performance by modifying several characteristics in real time. These systems can adjust parameters such as stiffness, ride height and damping in order to make a huge improvement in handling and comfort. To do so, they use an onboard actuator that is able to control the vertical and horizontal movement of the sprung mass with respect to the vehicle's wheel. This allows for continuous adjustments to the suspension forces and ride height, unlike the semi-active suspensions, which can only adjust damping values [5].

There are several types of active suspension systems, with one of the most common solutions being the hydraulic one. This solution uses hydraulic actuator to actively adjust the reciprocal position between vehicle and wheel. Some examples are the "hydractive" designed by Citroen [4] and the "Active Body Control (ABC)" designed by Mercedes [4].

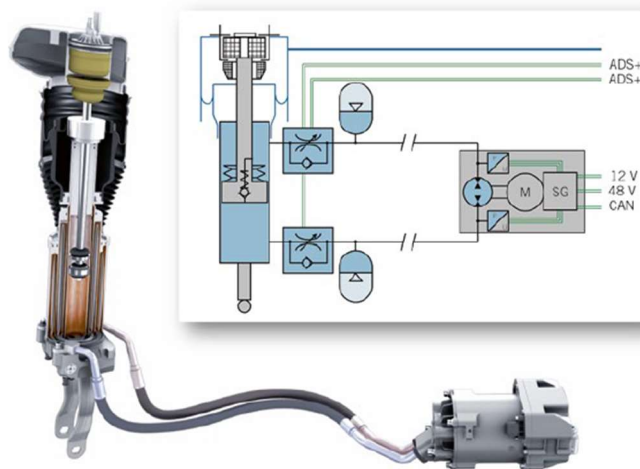


Figure 5 - Section view of the Active Body Control designed by Mercedes [6]

The ABC works together with the ‘road surface scan’, a sensor-equipped system detecting road irregularities. Depending on the condition of the road surface, the ABC system acts, via electro-hydraulic actuators, on the suspension characteristics, allowing adaptive regulation. In this way, safety and comfort conditions can be improved [6-7].

Another example of active suspension system is the electro-hydrostatic actuator (EHA). It consists of a hydraulic actuator driven by an external gear pump. The latter is coupled with an electric motor. The linear motion of the piston generates a fluid flow within the hydraulic circuit, which rotates the pump and motor shaft. Therefore, the electric machine can be controlled in order to yield the desired output torque, which is converted into a damping force by means of the same principle [8].

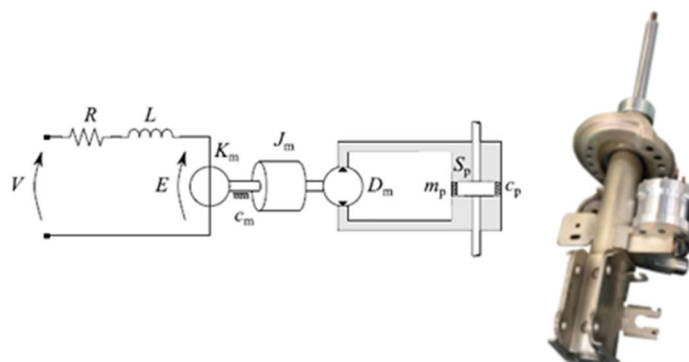


Figure 6 – EHA system layout [8] (left), EHA Prototype designed by PoliTO [9] (right)

1.1.3 Rotary regenerative shock absorber

The active and semi-active hydraulic dampers are usually used in top class vehicle segment due to the high cost. These suspension systems have as main drawback, being hydraulic, the oil presence. It is an issue when maintenance work needs to be done. In addition, these special fluids have the defect of deteriorating and losing their performance over the time. For this reason, the development of electromechanical dampers seems to be the most interesting solution among those currently available. The electromechanical dampers, with respect to the hydraulic competitors, on one hand have as drawbacks the weight and the high cost, but on the other hand they have several advantages [2]:

- Simplicity and reliability
- Small sensitivity to the environment parameters
- Small static friction
- Larger bandwidth

In addition, being able to work in all three configurations (active, semi-active and passive), they combine the typical characteristics of active and semi-active suspensions, i.e. adaptability and comfort, with the possibility of harvesting energy and actuating force into the suspension system. Indeed, when they work as passive shock absorber, they can harvest energy from road irregularities instead of wasting it as heat. In this way it is possible to improve the efficiency of the vehicle, and it results in reduction of the required power during the operation. Moreover, when the electromechanical dampers work in active configuration, they can put active forces into the suspension system. To this purpose they are equipped with an electric machine. Since the suspension motion has a linear nature, a linear electric machine is supposed to be the best choice for this system, but due to its limited force density, the best candidate is the rotative one [1-9]. From these assumptions comes the Rotary Regenerative Shock Absorber (RRSA). The electric motor can be controlled as a generator (damper) or as motor (actuator) [1-2]. When the motor is used as a generator, the rotation of the permanent magnets yields a time-varying magnetic flux linkage in the stator windings, thus inducing an electromotive force between the winding ends. If the circuit is shunted by a resistance, the electromotive force produces a force and hence a braking torque [8].

In these years more and more car manufacturers are investing in these technologies. Among them, in the 2016 Audi AG introduced eROT, a full active

electromechanical suspension system. This system combines the possibility of changing the damping coefficient and energy collection capacity with a highly compact structure [4].

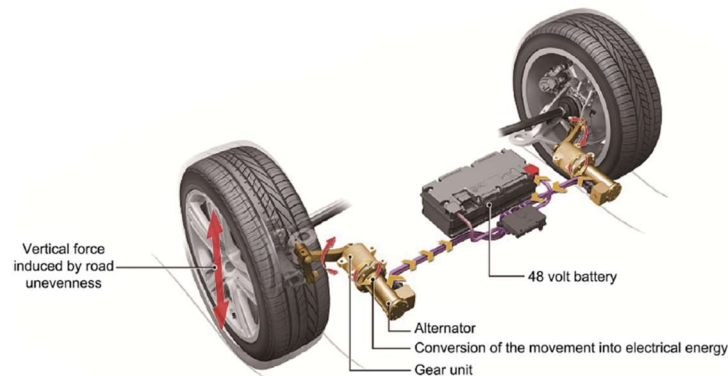


Figure 7 – eROT designed by Audi [4]

Having the suspension a linear nature, a linear-to-rotary conversion system is required [1-2]. Many possible configurations have been explored and analysed. For example, a ball-screw [10] and the rack pinion [11] system. In the end, the configuration that best meets the requirements is the one featuring a lever and a planetary gearbox.

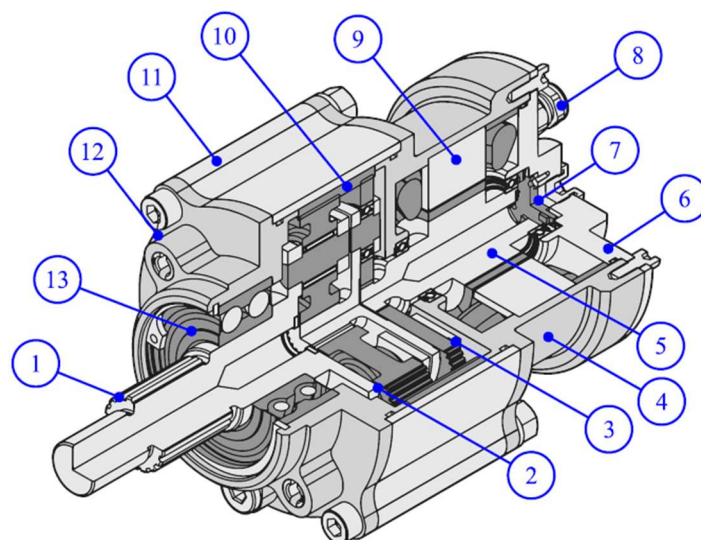


Figure 8 – Isometric cut view of the rotary regenerative damper prototype. Splined lever shaft (1), second stage (2), first stage (3), motor casing (4), rotor (5), back cover (6), angular position sensor (7), cable gland [x4] (8), stator (9), outer ring gear (10), gearbox casing (11), front cover (12), input bearing (13) [1]

The planetary gearbox is a widely used technology in the automotive industry and beyond. The main components of a planetary gearbox are:

- Sun Gear
- Planet Gear
- Ring Gear
- Carrier

Depending on which of these is fixed, the gearbox will work with a different transmission ratio. One of the most common solutions is to make the ring gear fixed and choose the carrier as input and the sun as output. The “Willis’ formula” allows to obtain the transmission ratio for all the planetary configurations. For the configuration at hand, it is simplified and becomes:

$$i = 1 + \frac{Z_{RING}}{Z_{SUN}}$$

The RRSA planetary gearbox, as shown in Figure 8, consists of two stages. Both stages are identical except for the gears’ width.

	Z_{SUN}	Z_{PLANET}	Z_{RING}	Planets Number	i_{stage}	$i_{gearbox}$	Gear’s width
1st stage	16	58	134	3	9.375	87.89	5 mm
2nd stage	16	58	134	3	9.375		15 mm

Table 1 – RRSA planetary gearbox features

1.2 NVH analysis methods for automotive applications

Nowadays, in automotive industry, the main aim is to obtain products which are cheaper, comfortable, and therefore better than direct competitors' ones. Within this competitive environment, acoustic comfort becomes increasingly important when choosing a vehicle. In this context NVH analysis gained a significant relevance.

A vehicle is an extraordinarily complex system obtained through the assembly of many components. Every car manufacturer (OEM) has his own system development lifecycle. In the last decades NVH considerations are more and more taken into account in the initial stage of the project. As it known, this allows to save money when it is necessary to implement a change [12].

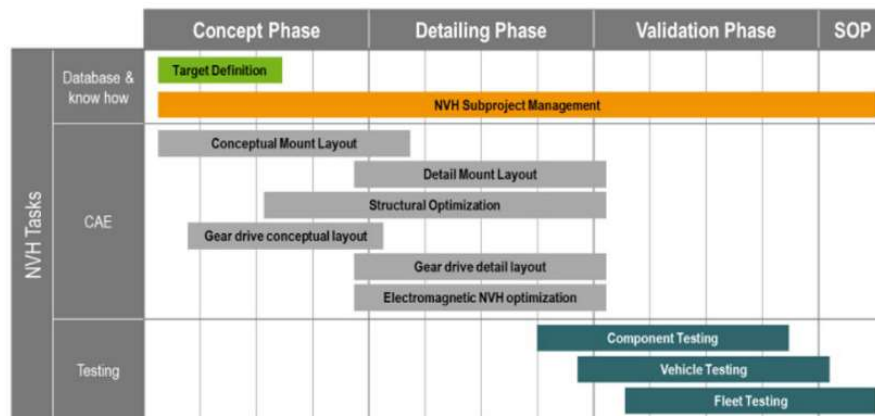


Figure 9 – NVH supported EDU development [12]

NVH stands for “Noise, Vibration and Harshness”. Noise is an unwanted sound inside or outside the car. It covers the whole audible range 20 Hz – 20 kHz; vibration is the excitation that goes into the passenger cabin; harshness is the most difficult to define. It is a term that describes the human’s subjective feeling to certain events. Harshness is created when a person’s subjective feeling is not in agreement with his expectations. For example, when a customer sees a smooth road surface in front of him, he expects a low level of vibration and noise. But if the road surface gives a higher level of vibration and noise, harshness feeling is created in the mind of the driver [13].

1.2.1 Structure-borne and airborne path NVH

Following a classification based on the transmission path, vehicle NVH is usually divided into two categories [14]:

- **Structure-borne NVH:** propagation of the vibration via all the “solid” parts of the vehicle between the source of the noise and the vehicle cabin (e.g. the engine mounts).

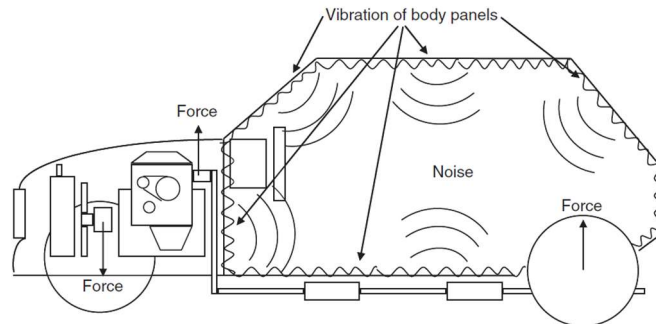


Figure 10 – Structure-borne paths [14]

- **Airborne NVH:** propagation of the source noise and vibration through via fluid medium (e.g. air); it comes into the passenger cabin through the leakages due to lack of sealing in the door or window.

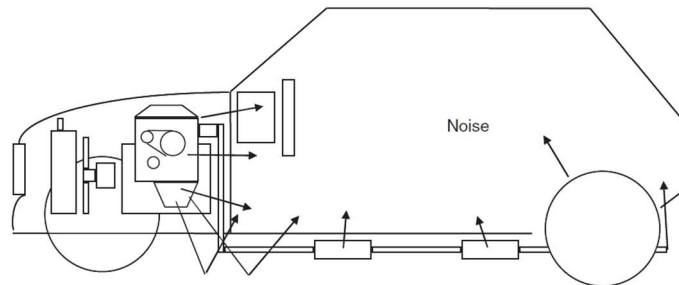


Figure 11 – Airborne paths [14]

Due to the vibration, the structure borne excitations could follow the air transmission path because of the sound pressure waves. Figure 12 shows a diagram of which are the transmission paths of the noise inside the vehicle.

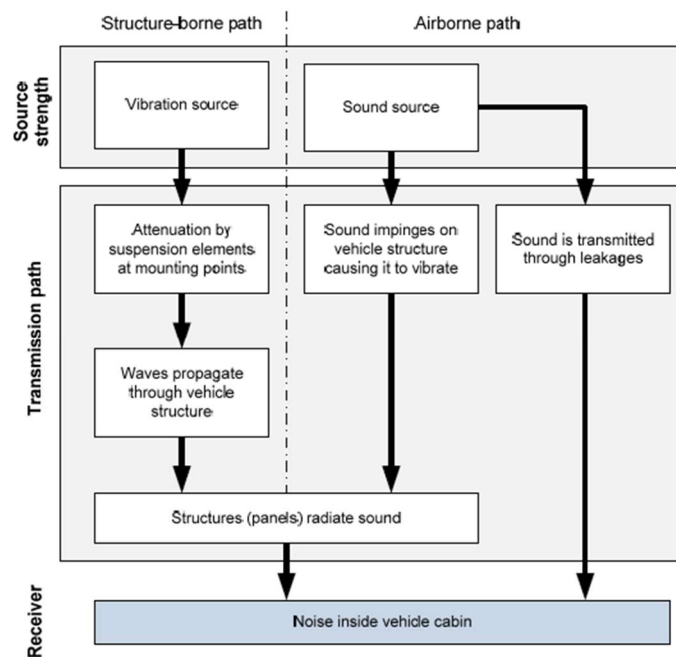


Figure 12 - Diagram of interior noise transmission path [15]

A lot of studies have demonstrated that, thanks to the vibration isolation treatment, such as engine mounts, the structure borne noises are all limited below a threshold frequency of 500 Hz. In this way, the vehicle NVH can be classified based on the frequency range. So, all the noises below 500 Hz will be “structure-borne noises”, while all the others will be “air borne noises” [13-15].

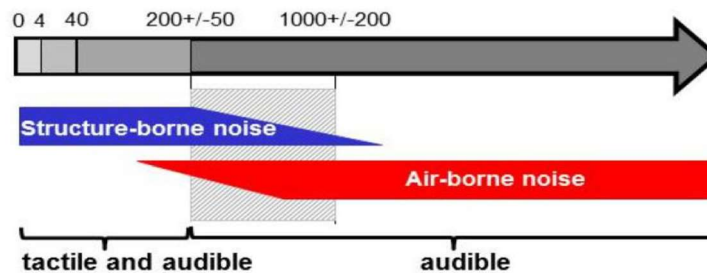


Figure 13 – Transition region between structure and airborne noise [16]

1.2.2 Noise sources in a passenger car

There are a lot of noise sources that affect the passengers in the car cabin. As it is possible to imagine, the first source of noise is the engine. The vibrations from the internal combustion engine (ICE) are mainly generated by the reciprocating and rotating masses. For this reason, it is particularly important to balance, as most as possible, these masses. These vibrations excite the motor panels, and their vibration generates noise, which in turn can reach the cabin

through the leakages. It has undergone a very deep analysis to minimize both his structural and airborne excitations [14-17]. Subsequently, after optimizing its NVH behaviour, the studies focused on other noise sources, such as road and aerodynamics noises [14].

- **Suspensions**

The suspension system is a crucial device for the vehicle. It allows to minimize the excitations that arrive from the road irregularities, so it has a role both in the dynamic behaviour of the vehicle and the NVH behaviour. Nevertheless, the suspension system itself make noise, especially the flow of fluid inside it.

- **Tyre**

The tyres play an important role because they are sources of both structural and air borne noise. The first one comes from the road irregularities and their stiffness can minimize these excitations. The latter are generated by the rolling of the tyre on the road. The tyre footprint could modify the level of noise.

In addition to road excitations themselves, also the resonant modes of the tyre and suspension can amplify the road forces. Depending on the working range, the tyres and the suspensions can work as a filter [13]:

- *Below 30 Hz*: the tyre works as a pure spring and the vibration inside the vehicle depends on the tyre radial stiffness.
- *Between 30-250 Hz*: the tyre modes (tyre radial, tyre transverse, tyre tangential) are active so, the tyre amplifies the force that comes from the road.
- *Above 250 Hz*: the tyre modes are damped.

- **Aerodynamics sources and wind noise**

The importance of the aerodynamics sources grows as the velocity increase. At higher speed it become one of the predominant sources. Following the behaviour of a dipole source, the intensity of the aerodynamic noise in a vehicle is proportional to the sixth power of the velocity [14].

It is possible to make a more detailed classification of noise sources inside a vehicle based on typical frequency ranges [13]:

- *Air borne powertrain noise*: it includes noise from engine, exhaust, and gears. The frequency range is 400-20000 Hz.
- *Wind noise*: it is generated by the wind passing through the vehicles. It is strictly linked with the travel speed. A speed change from 70 to 100 km/h turns into an increase of 5-7 dB.

- *Road noise*: it needs a special attention. The frequency range cover from 20 Hz to 1000 Hz, so it can be inserted both in the structure borne and, in the air borne ones. The Table 2 and 3 show how to consider it.

Road noise	Body drumming	Impact boom	Rumble noise	Rolling boom
Frequency range	20 – 125 Hz	20 – 125 Hz	20 – 125 Hz	20 – 125 Hz

Table 2 – Vehicle road noise classification [13]

Road noise	Tyre ring	Tyre path slap noise	Open hole noise
Frequency range	200 – 250 Hz	400 – 1000 Hz	400 – 1000 Hz

Table 3 – Vehicle road noise classification [13]

The reduction of the structure-borne noises is obtained using damping supports. The damping of each support (e.g. engine mounts) can be modified varying the material or the geometry. For example, it is possible to use several types of rubber. The main aim is to obtain a vehicle structure with an extremely low sensibility to the excitation force coming from the supports [14].

On the other hand, the reduction of the air borne noises can be obtained thanks to:

1. *Avoiding holes and leakages.*
2. *Working on the cabin structure.*
3. *Working on acoustic absorption inside the cabin.*

Focusing on the last point, it could be applied for the reduction of the structural borne noises, too. It is not convenient because the isolating materials show better performance at high frequencies (working range of the air borne excitations).

The capacity of sound isolation can be measured through the “Sound Transmission Loss”. This parameter allows to define the isolation capability of each structure/panel.

It can be calculated as follows:

$$TL(\beta, f) = 10 \log \frac{W_{in}(\beta, f)}{W_{out}(\beta, f)}$$

where:

β is the angle of incidence of the sound wave over the surface.

f is the frequency of the considered sound wave.

W_{in} is the sound power incident at the source side.

W_{out} is the sound power radiated at the opposite side of the partition.

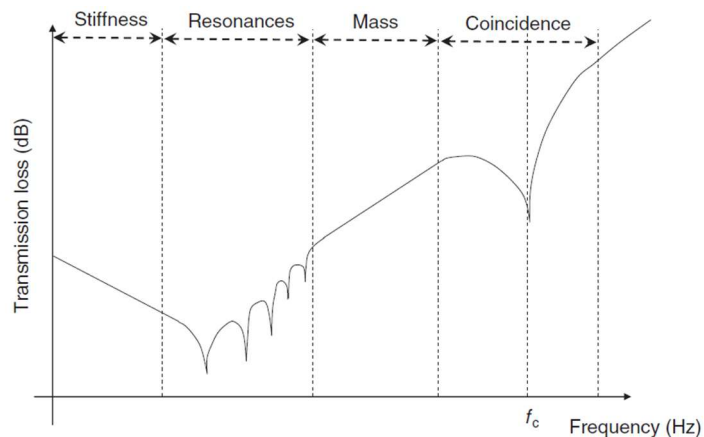


Figure 14 – Typical behaviour of the TL parameter [14]

From the diagram in Figure 14 it can be noticed that it is divided into four regions:

1. *Stiffness controlled region*: it is below the frequency of the first structure resonance mode. In this region the stiffness of the plates influences the level of the TL.
2. *Resonant region*: it is characterized by the resonances of the structure.
3. *Mass controlled region*: the TL level is governed by the mass of structure. The main feature of this region is that the TL increases by 6 dB for each doubling the mass or the frequency.
4. *Critical frequency*: it occurs when the length of an acoustic wave in air is coincident to the wavelength of the structural bending wave in the panel. In this case the TL drops to a very low value.

1.2.3 Experimental method in automotive environment: Transfer Path Analysis

The classification of the noise that comes into vehicle, as said, is based on how this happens. So, it possible to define the structural borne and the air borne noise. The main way to obtain this classification is the “transfer path analysis” (TPA). This method is used to rank the excitations and noises that come from system sources and go into a chosen location (cabin vehicle in this case). The transfer path analysis is an excellent way for NVH troubleshooting. It is based on the SPR (source-path-receiver) scheme. In the most NVH problems, the source is not known *a priori*, so a “trial and error” procedure is applied. There are many variations of this method, but the most used is the “experimental transfer path analysis”. It is a powerful tool that allows to determine which structural excitation is the predominant among all the excitation spectra [18].

The transfer path analysis has two main phases [18]:

- *Force estimation*: in the first phase, it needs to obtain the force acting on the structure.
- *Path analysis*: subsequently, it is possible to obtain the contribution of every single path, applying the estimated forces to the source-receiver transfer function.

To do this, it is convenient to rely on a matrix frequency response function (FRF) representation of the transfer function between a set of interconnection points and a set of target locations:

$$p = \sum \left[\frac{p}{F} \right] * F_{oper}$$

Where:

- p represents the sound pressure at specified locations.
- $\frac{p}{F}$ represents the vibro-acoustic transfer function between the source and the target location.
- F_{oper} represents the operational forces at the interfaces of interest.

In this case the target locations are the passengers’ ears. Instead, the forces of interest, for a suspension system, are the forces between the suspension and the vehicle body through the points of connection. As a result, the p/F functions are measured through the interface between the suspension interface and the passengers’ ears.

Since this is an experimental method, the sound pressure p and the vibro-acoustic sensitivities p/F can be measured directly. To populate the p/F matrix, the measurements must be done between the source and the target location without the source [18].

In short, the TPA method use a known artificial excitation, for example loudspeaker in the cabin for the airborne source or a shaker for the structural one, to obtain the FRFs of the source-receiver path. In this way, it is possible to measure the response at the receiver.

Once all these quantities are calculated, it is possible to rank the structure borne noise path. So, with the help of the previous equation, every single contribution will be calculated and within a coloured map it is possible rank them.

TPA method presents some drawbacks. First of all, the transfer paths must be measured one sub-system at a time. Additionally, each transfer path must be obtained singularly in order to avoid any “interferences” that could lead to contaminated results. Practically, it results in disassembling the system, namely it is very time consuming.

All these drawbacks have led to a new method, the “Operational Transfer Path Analysis”.

The **operational transfer path analysis** (OTPA) is a method developed by “Honda Research and Development” in the mid-2000’s [19].

The main difference between TPA and OTPA is that the first one determines a force-response transfer path relationship (FRFs), whereas the latter determines a response-response transfer path relationship (transmissibility).

The main advantage of the OPTA method over the TPA is that now, it is possible to obtain all the transfer path relationship simultaneously. It allows to save a lot of time. On the other hand, the main drawback is that the reliability of the response is closely linked to a properly setting up measurement. This is true also for the TPA method, but in the OTPA method an error in identifying all the correct source-receiver paths could not be so clear.

1.3 Noise and vibration sources in RRSA

In the last years, the development of the electric drive unit (EDU) has received a significant acceleration. The NVH analysis of vehicle powered by internal combustion engine (ICE) is focused on the noises and vibrations made by the engine itself. The engine, in fact, acts as a mask for the noises generated by other devices (suspensions, driveline, fan, etc.). When an EDU replaces the ICE, because of the high frequency tonal noise produced by the electric motor, all the noises coming from other devices becomes more and more important [20]. For this reason, in conjunction with the use of EDUs, an extended NVH analysis of other devices will also be conducted.

As shown in Figure 8, the rotary regenerative shock absorber (RRSA) consists of an electric motor and a two-stage planetary gearbox. A summary of the typical noises is reported.

1.3.1 Geartrain NVH

The typical noises generated by the geartrain are gear whine and gear rattle. The first one usually corresponds to the gear mesh frequency and its harmonics. It must be studied very carefully.

The **gear whine** noise is mostly due to [12]:

- *Transmission error*: it represents a measure of the difference between the driven gear's rotational velocity and the perfect conjugate action. It depends strongly on the tooth geometry, gear manufacturing quality and assembly errors.
- *Dynamic mesh force*: it is a force in the meshing contact point. It is dependent on the existing of the transmission error.
- *Force transmissibility*: it represents the quantity of dynamic mesh force transmitted from meshing zone to the bearings and mounting locations.
- *Body acoustic sensitivity*: it represents the airborne and structural borne noise transfer function from the mountings to the passenger cabin.

The **gear rattle** is a typical noise of transmissions with large time-varying high-torque load. Due to backlash, the gears can lose the contact and then regain it on impact. Rattle can be reduced by appropriate sizing of the meshing clearance and reducing the effects of excited resonances by tooth impacts [21].

1.3.2 Electric motor NVH

The electric motors mainly produce two kinds of noises: electromagnetic and mechanical ones. Despite being relatively low in intensity, these noises can be particularly unpleasant due to their tonal and high-frequency nature [12].

The **mechanical noises** originate from issues linked with the rotor. It is possible to divide it:

- *Rotor unbalance*: when the rotor's mass is not perfectly distributed, it leads to vibrations and noise.
- *Rotor misalignment*: it can be either angular (rotor is tilted) or parallel (rotor is shifted).

In the same way, it is possible to recognize **electromagnetic noises**. They are linked to the air gap between the stator (stationary part) and the rotor (rotating part). The main parameters influencing electromagnetic noise are:

- *Air gap*: this space could generate noise if it is not uniform.
- *Number and type of slots*.
- *Winding distribution*.
- *Radial forces*.

The main electromagnetic noise sources are:

- *Cogging torque*: this is caused by the interaction between the rotor's permanent magnets and the stator's slots, leading to a non-uniform motion that generate noise.
- *Ripple torque*: the variation of torque production by the motor could create oscillations, contributing to noise.

1.4 Thesis outline

Chapter 1 provided an overview of the key differences between semi-active and active suspension systems. It also highlighted the unique features of electromechanical dampers, such as RRSA. Lastly, the chapter offered an overview of the methods used in the automotive industry for NVH analysis. After concluding this introduction section, it is possible to move on the objective of this thesis, which is to carry out an NVH analysis of the Rotary Regenerative Shock Absorber. It will be subdivided as follows:

- **Chapter 2:** in this section a comparative analysis will be carried out between two different RRSA prototype. Both prototypes share the same electric motor but differ in gearbox configuration. The starting model is equipped with a planetary gearset with spur gear; it will be compared with a prototype equipped with cycloidal gearbox. This comparison addresses both vibrational and acoustic contribution. In addition, it will be made both for active and regenerative mode. Finally, a summary will be reported considering the efficiency and size of both prototypes.
- **Chapter 3:** in this section a quick look at the main simulation methods used in the automotive industry. Subsequently, a simulation model of the planetary RRSA is analysed. This simulation analysis is conducted with the software “Excite M” by AVL®. Through this model, simulations can be carried out in order to understand what modifications can be made to achieve improvements in acoustic performance. Finally the results are compared with respect to the Galluzzi’s tests.

2 Experimental analysis: planetary vs cycloidal RRSA

A new RRSA solution, equipped with cycloidal gearbox, has been developed. To assess its performance, a comparative analysis with the previous solution is conducted, which includes a detailed NVH study.

A first initial acoustic analysis has been carried out in 2021 by Galluzzi et al. [1]. The tests have been conducted in an anechoic room. The test bench was different from the one used for this study. It was equipped with two microphones, the first on the side of the prototype and the second in front of it. There was also a foam pad in order to isolate the RRSA from the support structure.

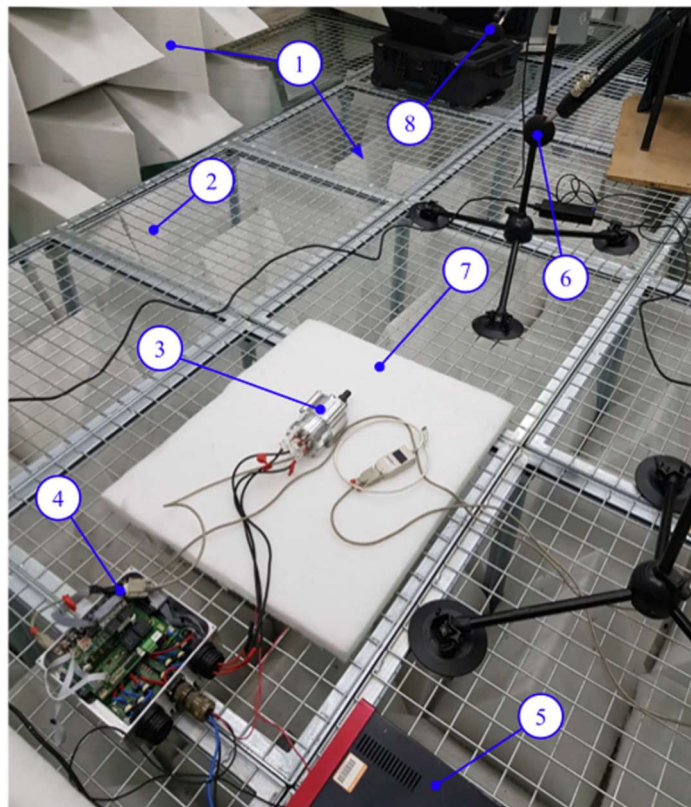


Figure 15 – Previous acoustic characterization setup: wall and floor foam blocks (1), supporting structure (2), rotary regenerative damper prototype (3), prototype control unit (4), power supply (5), side microphone (6), foam pad (7), front microphone (8). [1]

In this test setup, the RRSA was driven as a motor using a power supply, controlled with constant and sinusoidal speed references. It is important to emphasize that the RRSA has no applied load.

2. Experimental analysis: planetary vs cycloidal RRSA

Input type	Speed		Lever Speed	Rotor Speed	RMS SPL [dB(A)]	
	Amplitude [mm/s]	Frequency [Hz]	[rpm]	[rpm]	Front	Side
Constant	96	-	7.97	696.32	36.03	36.92
	178	-	14.78	1291.09	42.3	44.08
	341	-	28.32	2473.38	47.89	49.63
Sinusoidal	41	2	3.40	297.39	37.07	35.23
	62	1.5	5.15	447.71	37.01	37.36
	328	1	27.24	2379.09	46.97	48.69

Table 4 – Measured SPL with constant and sinusoidal input speeds. [1]

As it is possible to see, the side RMS SPL values are slightly higher than the front ones. This difference is due to the emitting surface of the RRSA, which is considerably larger for the microphone placed on the side than for the microphone placed in front.

Based on these findings and with a focus on optimizing acoustic performance, new design possibilities for the rotary speed reducer were explored. The chosen solution involved developing a prototype equipped with a cycloidal speed reducer. **Cycloidal speed reducers** are becoming more and more popular in various industries due to their specific features. In fact, its unique working principle brings with it several advantages. It is composed by four different parts, as shown in Figure 16: a high-speed input shaft, a cycloidal disk, fixed pins and a low-speed output shaft. The operating principle is as follows: the eccentric input shaft drives the cycloidal disk that, engaging with the fixed pins, rotates both with the eccentricity and around its symmetry axis. Subsequently, through the engaging between the rollers and the disk holes, the second movement is transferred to the output low-speed shaft. The output shaft will result coaxial with the input shaft, but the rotating movement is opposite respect to the input shaft [22].

The reduction ratio can be evaluated by the formula [23]:

$$i = \frac{\omega_{in}}{\omega_{out}} = -\frac{n}{N - n}$$

2. Experimental analysis: planetary vs cycloidal RRSA

where:

N: number of fixed pins

n: number of lobes of the cycloidal disk.

The tested prototype has eighty-eight fixed pins and the fixed pins' pitch radius is equal to 60 mm [22]. The main parts of a cycloidal reducer are shown in Figure 16.

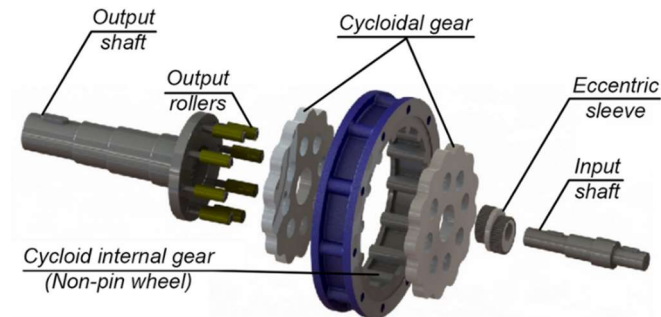


Figure 16 – Disassembled single-stage Cycloidal reducer view [24]

In addition, this technology should guarantee superior noise performance. A table comparing the expected results is presented below.

	Cycloidal drive	Planetary gearbox
Efficiency	4/5	5/5
Noise	5/5	3/5
Axial size	5/5	3/5
Radial size	3/5	4/5

Table 5 – Anticipated results cycloidal vs planetary [22]

2.1 Test bench configuration

An experimental campaign is carried out to have a direct comparison between the two reducers on both energetic and NVH performances. The test bench is provided with accelerometers and microphones. In order to be able to examine the full potential of the RRSA, in both active and regenerative mode, a servo motor, the Kollmorgen® DBL5-1700 brushless PM motor, is coupled to it via a toothed belt transmission with a 2:1 ratio. The toothed belt (HTD8M) is properly preloaded to match a maximum input torque of 160 Nm. In Figure 17, it is possible to see the test bench configuration.

2. Experimental analysis: planetary vs cycloidal RRSA

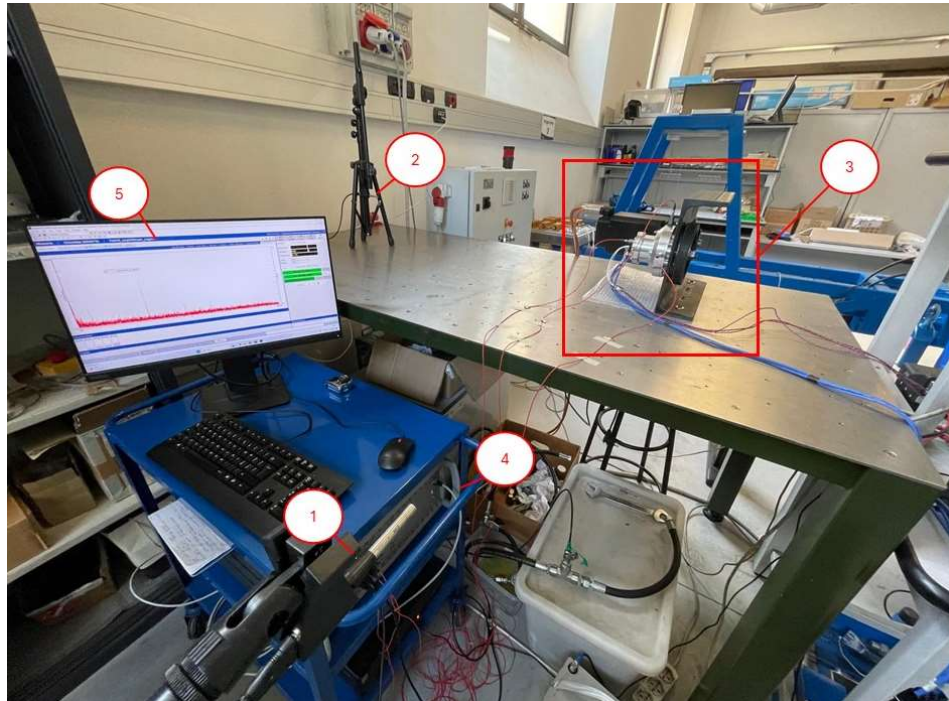


Figure 17 – Test bench configuration: microphone A Side (1), microphone B Back (2), Flange support (3), SCADAS LMS (4), PC acquisition (5)

Focus on the flanged support of the test bench is reported.

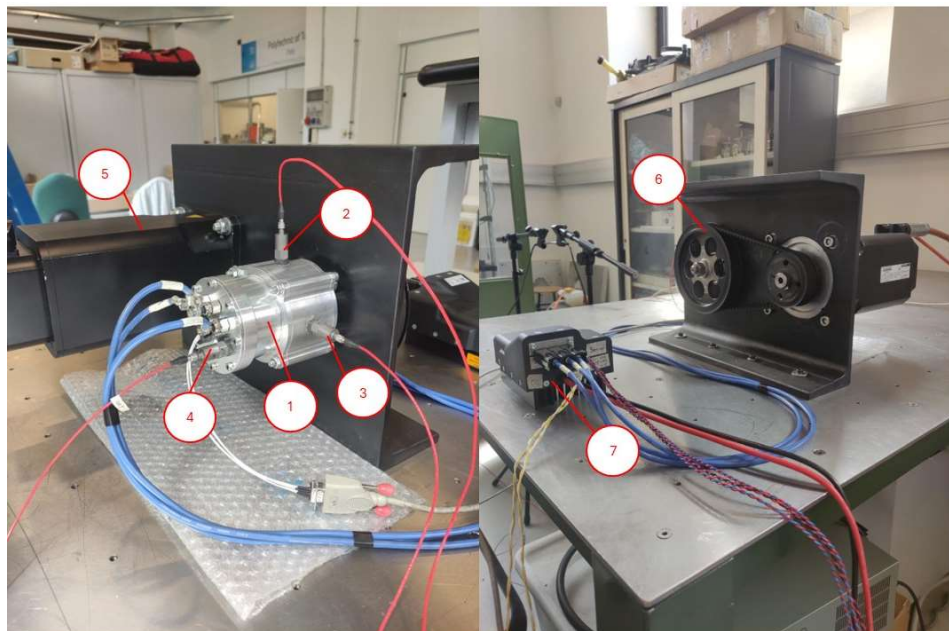


Figure 18 – Test bench configuration focus: RRSA prototype (1), accelerometer Top (2), accelerometer Lateral (3), accelerometer Motor (4), Kollmorgen® (5), belt-pulley transmission (6), inverter RRSA (7)

2. Experimental analysis: planetary vs cycloidal RRSA

For a comprehensive NVH analysis, the use of microphones and accelerometers is essential. As with the previous test bench configuration [1], two microphones (AVM® MI 17 “free-field”) are positioned one meter away the rotary regenerative shock absorber: the first placed in front of the RRSA, facing the electric motor, while the second on the side of the prototype in the direction of the planetary gearbox.

On the other hand, to acquire the vibration contribution, three different accelerometers (PCB Piezotronics®) are placed all over the prototype. One on the top, one on the side and the last on the back of the rotary housing.

All these data are processed thanks to the SCADAS LMS III designed by Siemens®. The SCADAS is a hardware designed specifically to acquire data from various devices such as microphones and accelerometers. Once the signal is received by the sensors, the SCADAS performs the signal conditioning. It consists of converting signal from analogic to digital form. Simultaneously, amplification and filtering of it is carried out. Finally, the acquired data are transferred to a PC data acquisition, where a software, in this case Simcenter Testlab powered by Siemens®, allows to elaborate the data.

The schematic view of the entire test bench is shown in Figure 19, in order to better explain the configuration.

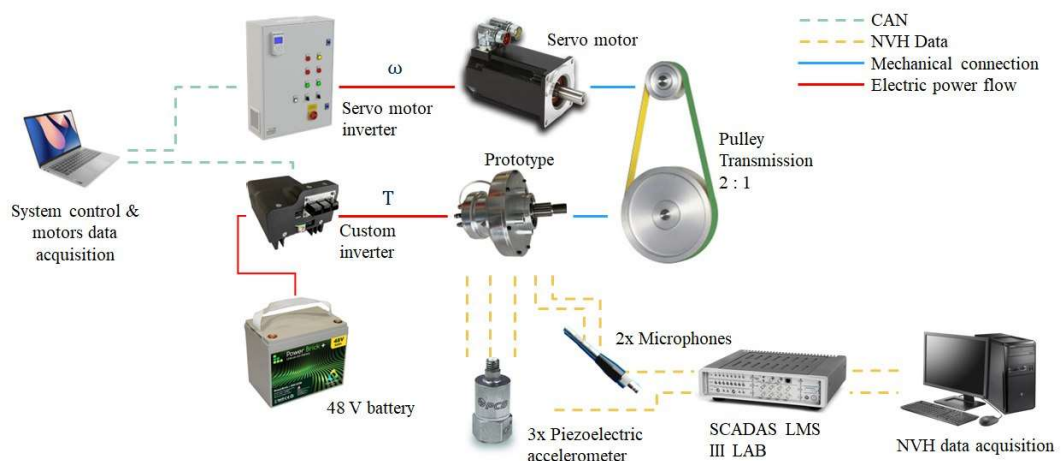


Figure 19 – Schematic view of the entire test bench

The results are then further analysed and post-processed in the MATLAB environment.

2. Experimental analysis: planetary vs cycloidal RRSA

2.1.1 Test bench Impact Testing

The test bench is characterised through an ‘impact test’. In this way, the Frequency Response Function (FRF) of the test bench is obtained. It represents the relationship between the structural response and the applied excitation. To achieve this, an impact hammer (PCB Piezotronics® model 086C03, see Figure 20) is required in addition to the previously set equipment.



Figure 20 – Impact Hammer PCB Electronics®

Several points of the test bench are hit, as shown in Figure 21.

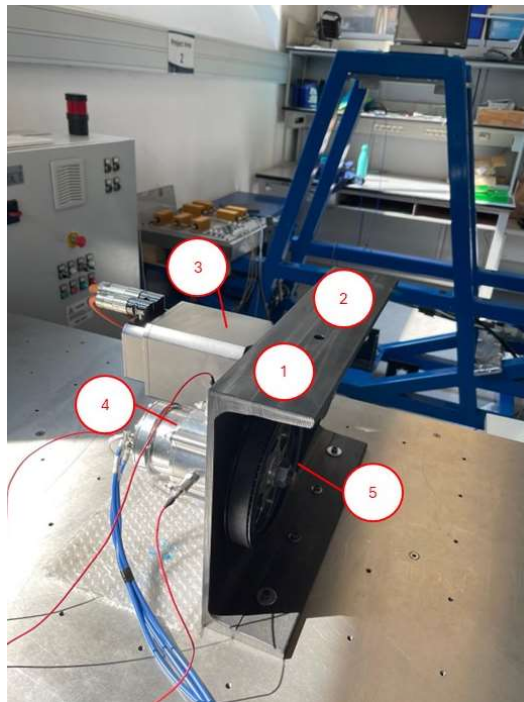


Figure 21 – Impact test points

2. Experimental analysis: planetary vs cycloidal RRSA

In this case, the applied excitation is the hammer force, and the structural response is the acceleration measured by the “accelerometer Top” (number 2 in the Figure 18):

$$FRF = \frac{\text{Acceleration "Top Accelerometer" [g]}}{\text{Impact hammer force [N]}}$$

The most remarkable results are obtained by hitting the flange support in the point 1 or 2 in Figure 6. The results obtained are shown in Figure 22.

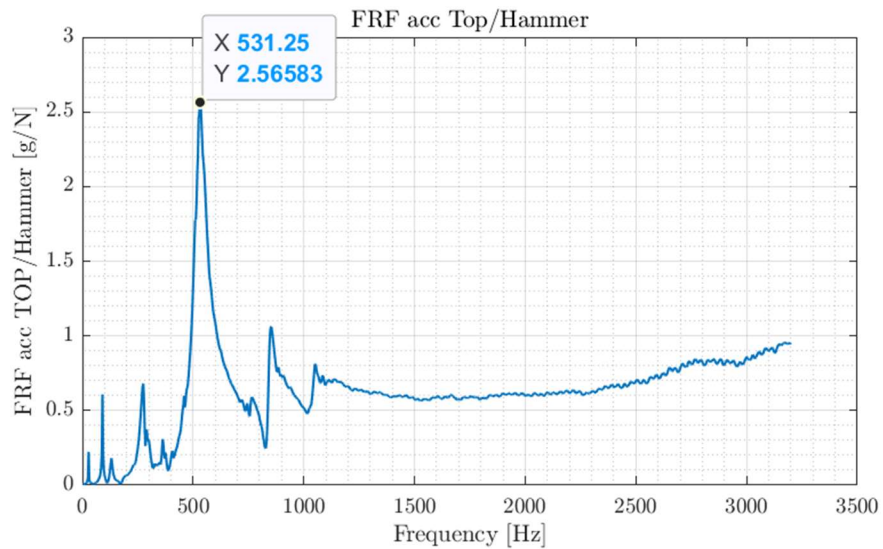


Figure 22 – FRF Flange spot

The results in Figure 23 show also a good coherence.

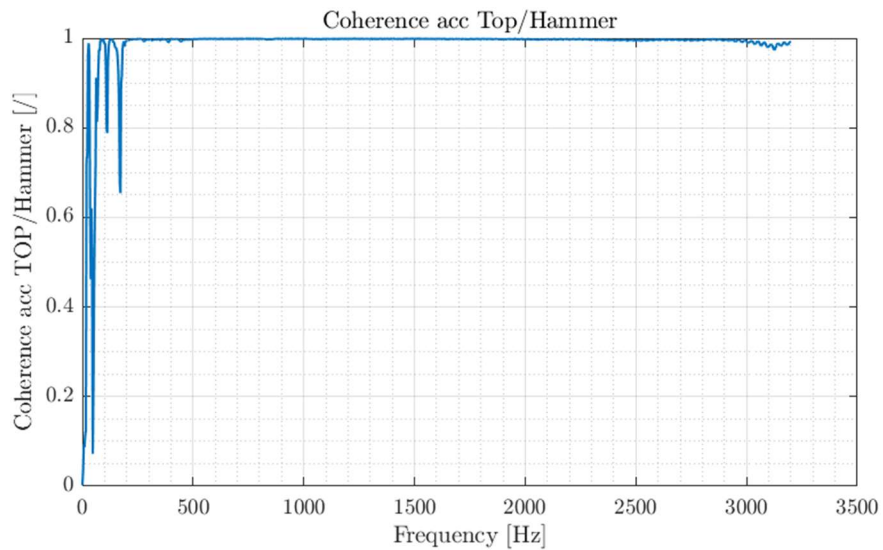


Figure 23 – Coherence Flange spot

Figure 22 shows a peak in the frequency around 500 Hz. These results will be further considered when the vibrational analysis will be carried out.

2.2 Test procedure

As explained in the previous paragraphs, this test campaign is carried out for obtaining both NVH performances and system efficiency. The tests are conducted controlling both the RRSA prototype and the Kollmorgen®. The main Input/Output data are:

- Input
 - Kollmorgen® controlled in constant speed from 500 to 3500 rpm by steps of 500 (controlled via CAN).
 - Rotary controlled in torque with a ramp from 0 Nm to 1.5 Nm (at the electric motor level) in 15 seconds (controlled via CAN).
- Output
 - Both speeds.
 - Both torques (esteemed by current sensors).
 - I_{DC} and V_{DC} of the rotary battery.

Here below a plot of the input and output quantities of the test procedure is reported.

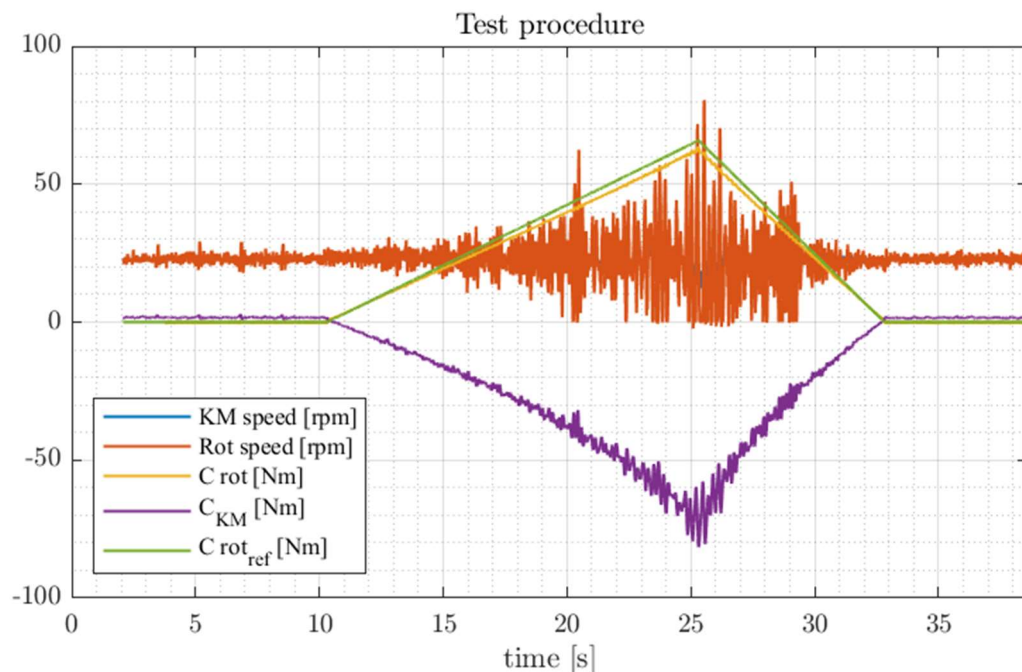


Figure 24 – Test procedure quantities

In Figure 24 the data are standardized by applying the appropriate transmission ratio to ensure consistency. All data are aligned to the Kollmorgen® shaft.

2.3 Test results

The NVH analysis in this thesis compares two different prototypes: one with a planetary gearbox and the other with a cycloidal gearbox. Both the prototypes share the same electric motor, allowing for a focused comparison of the differences between the gearboxes.

2.3.1 Planetary prototype results

A brief introduction about state of the art for NVH analysis of planetary reducers is needed to better understand the following results. A spectrum analysis usually exhibits some relevant frequencies [25-26]:

- *Gear mesh frequency (GMF)*: it is related to the gear meshing.
- *GMF sidebands*: some sidebands of the main GMF might arise.
- *Electric motor frequencies*: related to the electromagnetic forces at the air gap, which excite the air gap and thus the case of the prototype.
- *Bearing frequencies*: these frequencies, usually, are related to some defects on the roller elements or on the rails.

The aim of these experimental campaign tests is to compare, as said, two different prototypes that differ only for the speed reducer typology. For this reason, the electric motor frequencies will not be further explored.

The GMF and the related sidebands will be calculated [24]:

$$GMF = z_r * \frac{n_c}{60} = \frac{z_r * z_s}{z_r + z_s} * \frac{n_s}{60}$$

where:

- z_r is the number of ring teeth.
- z_s is the number of sun teeth.
- n_c is the carrier speed in RPM.
- n_s is the sun speed in RPM.

The sidebands are related to the rotating speed of the input shaft and output shaft. These can be obtained [25]:

$$f_{s,input} = \frac{n_{input} [rpm]}{60}$$

2. Experimental analysis: planetary vs cycloidal RRSA

$$f_{s,output} = \frac{n_{output}[rpm]}{60}$$

Following these equations, the results obtained for the planetary prototype, subject of this thesis, are reported in the following table.

Rotor Speed [rpm]	GMF first stage [Hz]	Input Shaft frequency [Hz]	GMF second stage [Hz]	Input Shaft frequency [Hz]
500	119.1	8.3	12.7	0.9
1000	238.2	16.7	25.4	1.8
1500	357.3	25	38.1	2.7
2000	476.4	33.3	50.8	3.6
2500	595.6	41.7	63.5	4.4
3000	714.7	50	76.2	5.3
3500	833.8	58.3	88.9	6.2

Table 6 – Gear mesh frequency for every studied case

The sidebands will have a frequency range of:

$$GMF_i \pm k * f_{s,input}$$

$$GMF_i \pm k * f_{s,output}$$

where:

- $i = 1, 2$ indicates the stage of interest.
- $k = 1, 2, 3, \dots$ is an integer, and it indicates the number of sidebands considered.

The gear mesh frequency is intimately linked to the concept of order; they are essentially two aspects of the same phenomenon. In fact, finding the gear mesh order is straightforward. It is calculated by dividing the GMF of the stage by the rotational frequency of the input shaft. So, for this prototype:

- Gear mesh order of the first stage is equal to 14.29
- Gear mesh order of the second stage is equal to 1.52

With this section completed, the following paragraphs will present and analyse the results obtained from both vibrational and acoustic tests.

2.3.1.1 Planetary vibration analysis

The trends and results, obtained for both prototypes, across different speed steps (500, 1000, 1500, etc.) are consistent. Therefore, the results for the 2000 rpm case are presented as representative of the overall findings.

Starting from the raw data obtained from the accelerometer, a fast Fourier transform (FFT) is performed.

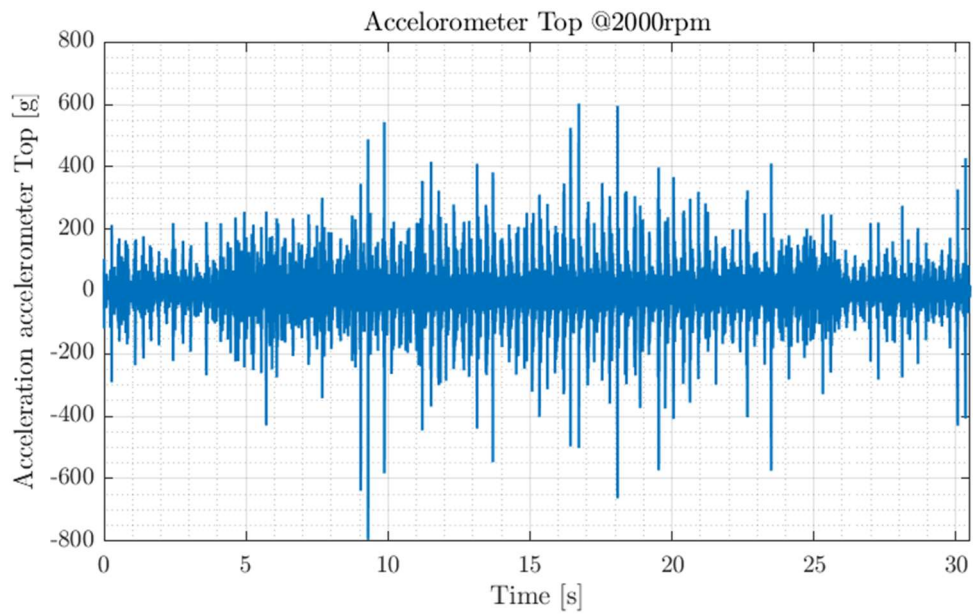


Figure 25 – Accelerometer Top raw data in time domain

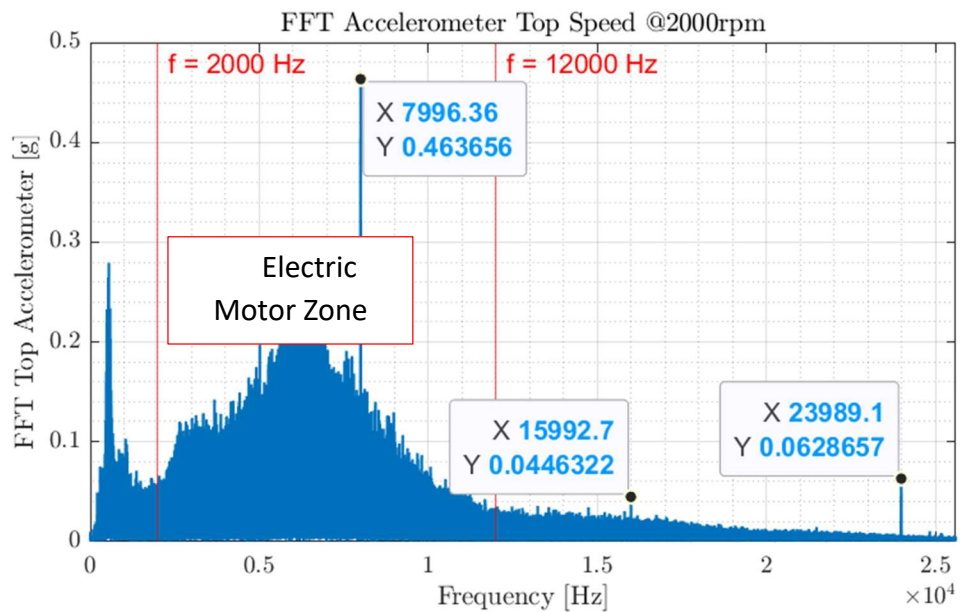


Figure 26 – FFT Accelerometer Top

2. Experimental analysis: planetary vs cycloidal RRSA

The first thing that stands out is the peak at 8000 Hz (highlighted by the first red circle). As shown, this peak includes the second harmonic (twice the main frequency) and third harmonic (three times the main frequency), both circled in red. This peak is due to the Kollmorgen® inverter, since it was present also at standstill and presents the same frequency of a whistle coming from inside its inverter. Hence, it is unrelated to the prototype itself.

The second thing of the spectrum that is possible to notice is the presence of two distinct zones. There is a great zone with a hilly trend that goes from 2000 Hz to 12000 Hz. All these excitations come from the RRSA and the Kollmorgen® electric motor. In fact, as mentioned in the previous paragraphs, the electric motor, unlike the internal combustion engine, produces tonal noises that are in a high frequency range. Consequently, for the purposes of this study, this area is not further investigated.

The last and the most important zone for the purpose of this study is the first one that goes from 0 Hz to 1500 Hz. As said before, this is the typical frequency range affected by the gearbox vibration of the planetary prototype. A further analysis of this frequency range is carried out.

The post-processing of the data in order to highlight the frequency range from 0 to 1500 Hz is conducted for a limited portion of time in the torque ramp area, as shown in Figure 27, where the interested time period is delimited by yellow lines.

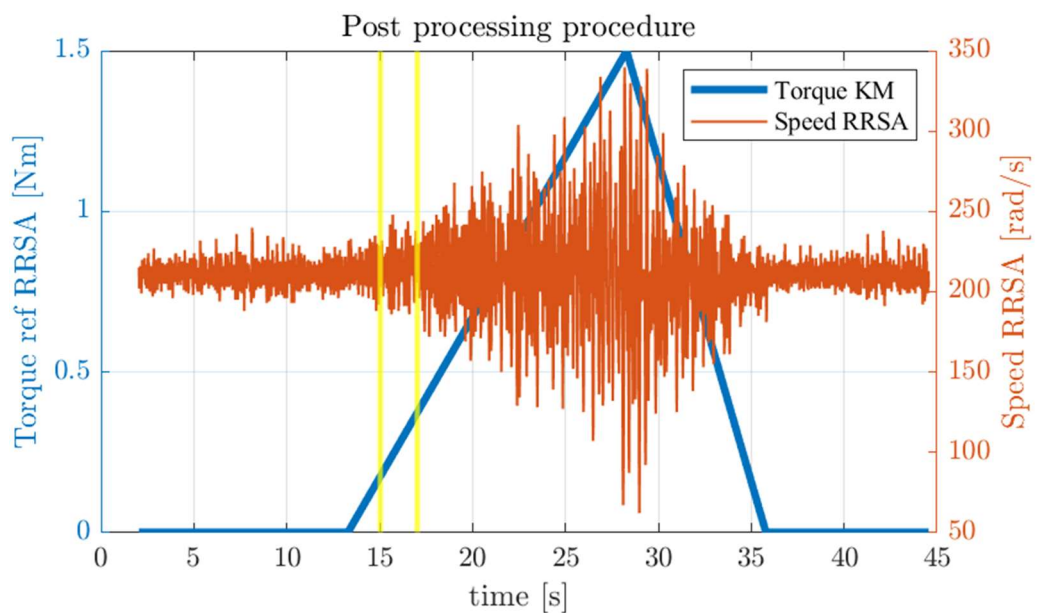


Figure 27 – Spectrum considered in torque ramp

2. Experimental analysis: planetary vs cycloidal RRSA

In fact, as reported in the test procedure paragraph (Paragraph 2.2), the RRSA is controlled in torque mode with a ramp that goes from 0 Nm to 1.5 Nm. The signal from 15 seconds to 17 seconds is isolated. This specific time range is selected to focus on the portion of the test where the prototype works under load. As shown in Figure 27, for higher torques the velocity becomes unstable, making it not optimal for order analysis. The obtained FFT is described in the following figure.

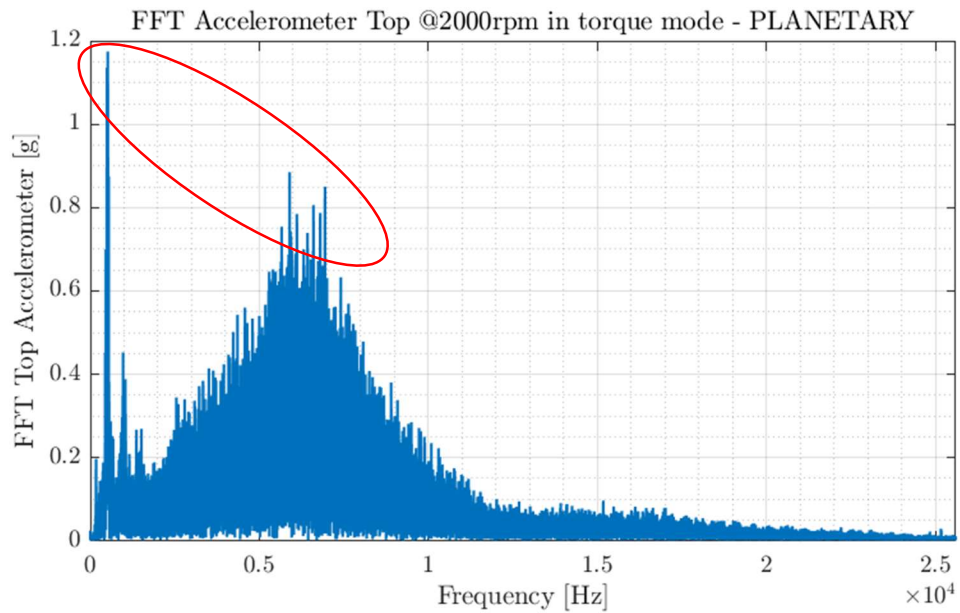


Figure 28 – FFT for a RRSA in torque ramp area

Figure 28 clearly shows that the excitations related to the mechanical components of the RRSA overcomes those related to the electrical part becoming predominant factor. Obviously, the entire spectrum exhibits higher values. In fact, in this case on the Y axis it is possible to see that it reaches levels between 1g and 1.2g, whereas in figure 26 the maximum values were only around 0.25g to 0.3g.

A more in-depth analysis will be done. It is necessary to focus on the frequency range between 0 Hz and 1500 Hz.

2. Experimental analysis: planetary vs cycloidal RRSA

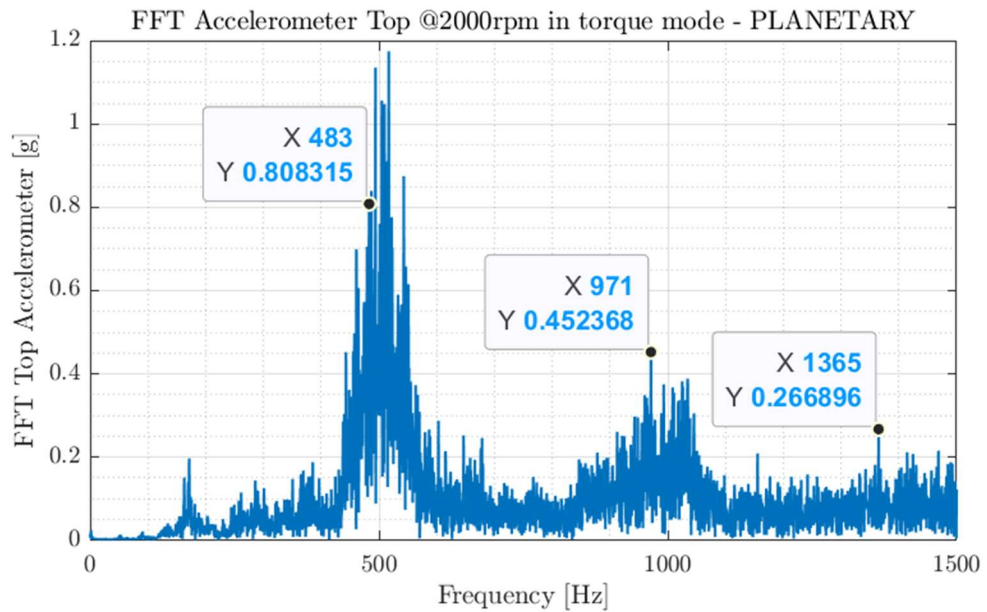


Figure 29 – FFT analysis between 0 Hz and 1500 Hz

In Figure 29, some points are highlighted. As reported in table 6, the first stage GMF of the RRSA is equal to 476.4 Hz. Consequently, some peaks around 476 Hz is expected to. The main peaks will be now analysed:

- The first peak around 170 Hz is something related to the test rig. In fact, it is possible to notice this peak for all the different tests. Ultimately, it is possible to say that it is not related to the prototype itself. Moreover, its magnitude is very small.
- In the frequency range between 450 Hz and 550 Hz, it is possible to see a lot of peaks. Among them, a peak around 480 Hz is highlighted. It is related to the first stage GMF and its sidebands. All the other peaks will be better explained later.
- The second and the third harmonic of the GMF is expected to be around 950 Hz and 1400 Hz. In this figure, the last two peaks highlighted are probably the second and the third harmonic.

The analysis conducted so far refers to a single case, specifically the one at 2000 rpm. Analysing all the other cases, it is possible to obtain the waterfall plot in Figure 30.

2. Experimental analysis: planetary vs cycloidal RRSA

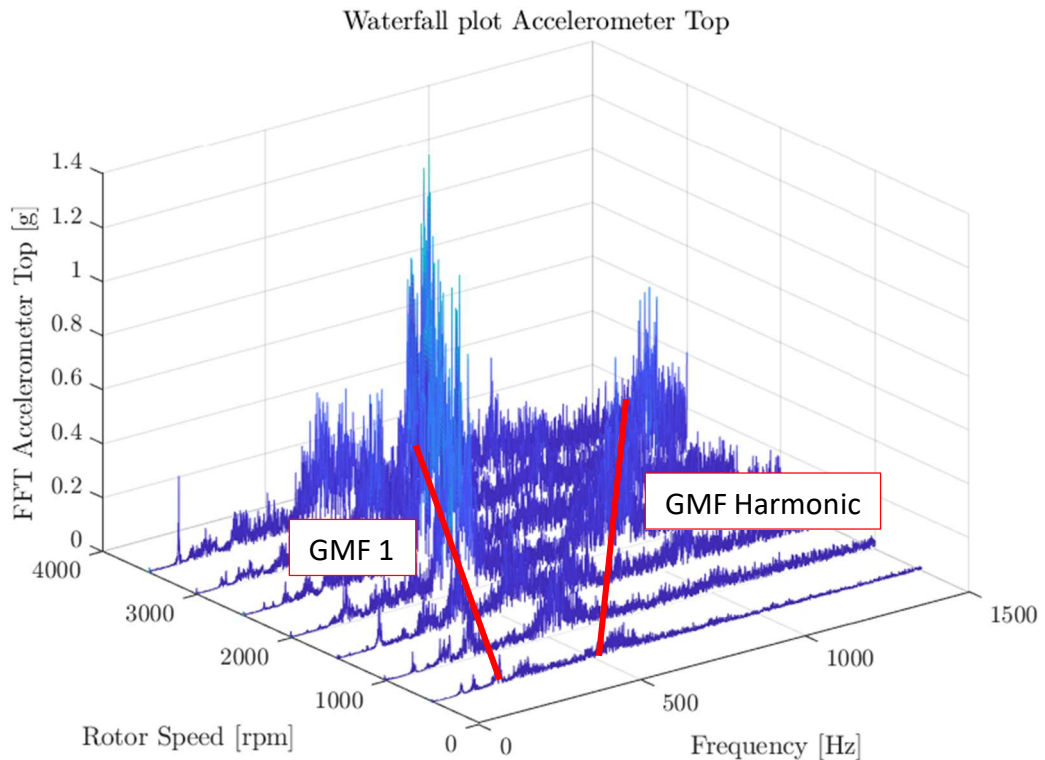


Figure 30 – Waterfall plot

Figure 30 shows clearly the Gear Mesh Frequency of the 1st stage and its second harmonic. This is the expected pattern. Obviously, it is possible to see that the spectra are not very clean. As explained previously, this is due to the resonance of the test rig. As shown in Figure 18, in addition to the RRSA, the test bench is also equipped with an external motor (Kollmorgen®) and a belt-pulley transmission. Everything is connected via a flange. As a result, all vibrations coming from the Kollmorgen® will first be transferred to the flange and then to the prototype.

2.3.1.2 Planetary acoustic analysis

Having completed the vibrational analysis, it is possible to move on to the acoustic analysis. It is carried out for both the active mode and regenerative mode. In this way, a complete comparison is obtained.

Usually, the main parameter that is used to define acoustic performance is Sound Pressure Level (SPL). The concept of level is useful when the quantity

2. Experimental analysis: planetary vs cycloidal RRSA

under consideration varies by several orders in time. This is the case with sound pressure [27]. The SPL is defined as:

$$SPL [dB] = 20 * \log\left(\frac{p_{measured} [Pa]}{p_{ref} [Pa]}\right)$$

where the p_{ref} is equal to 20 μ Pa.

- **Active mode**

Starting from the pressure acquired from the microphones during the tests, a complete acoustic analysis in order to obtain the sound pressure level is carried out. Here below the results are reported.

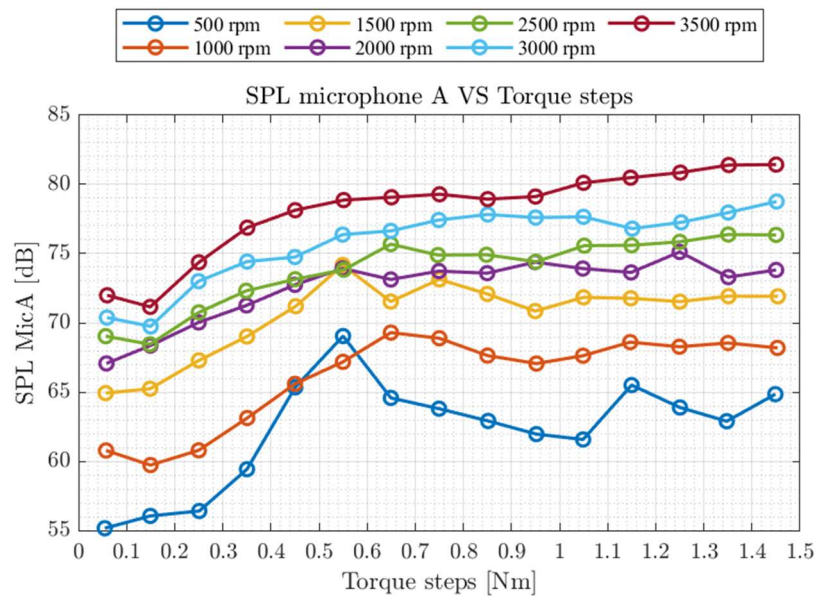


Figure 31 – SPL Microphone A in dB

Figure 31 is generated by isolating the torque ramp from the full test. Subsequently, the ramp torque has been divided into 15 steps of 0.1 Nm and the Root Mean Square (RMS) of the signal for each torque is computed. Finally, for each RMS value, the SPL is calculated. In Figure 31 it is possible to see the same pattern for all the speeds, apart from 500 rpm, which has a strange pattern due to the test rig. In fact, during the test, the latter has shown some problems on speed and torque control of the Kollmorgen® and of the RRSA. The 500-rpm test was very critical as the Kollmorgen® was controlled at a very low speed, due to the transmission ratio.

2. Experimental analysis: planetary vs cycloidal RRSA

A further representation is reported now. It is an acoustic performance map, and it is obtained by interpolating on a finer mesh grid.

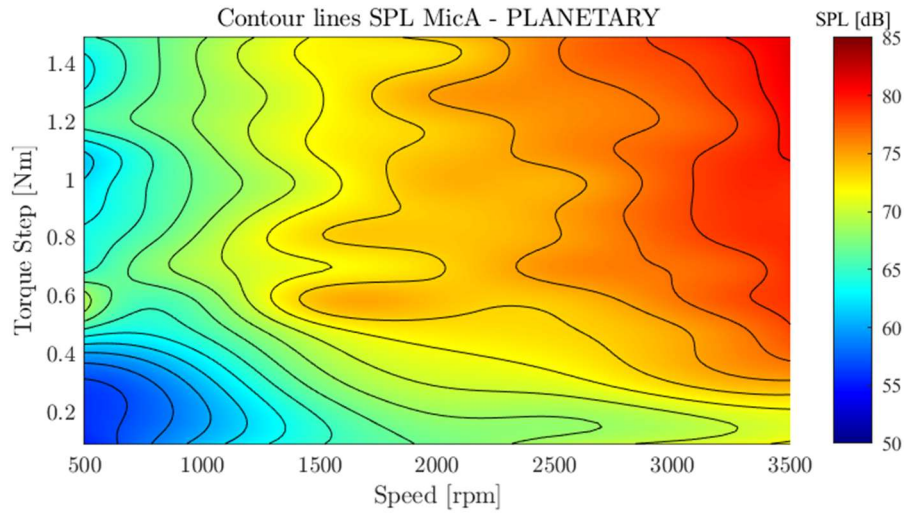


Figure 32 – Contour lines plot SPL microphone A

This contour lines plot is derived from the postprocessed results shown in Figure 31. In addition, a bi-dimensional interpolation, using the “spline” interpolation method, has been carried out to enhance the smoothness of the data. The aim of this plot is to represent an acoustic performance map in order to understand in which speed and torque range there are the worst results.

Another possible type of representation is in the frequency domain. In this way, it is possible to see which frequency ranges are most excited. Here below third octave bands plots for the microphone A and B are reported.

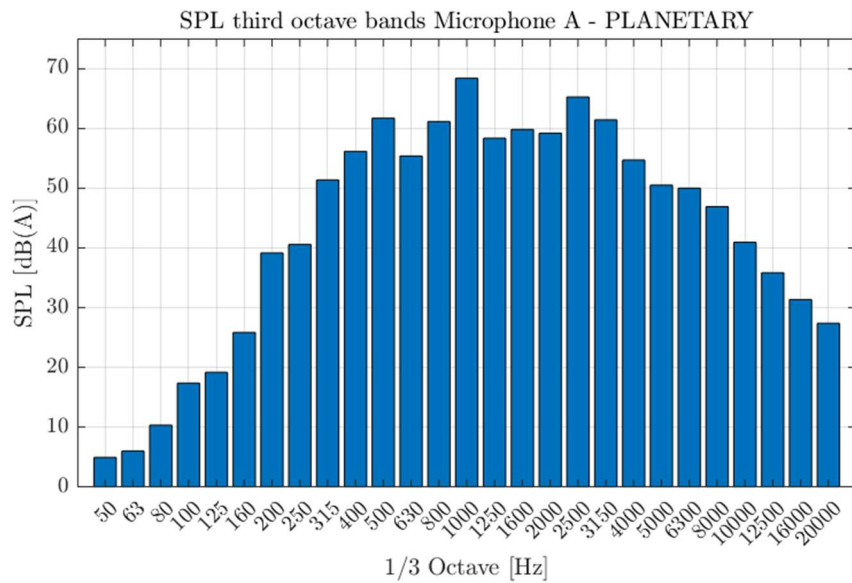


Figure 33 – Third octave bands microphone A

2. Experimental analysis: planetary vs cycloidal RRSA

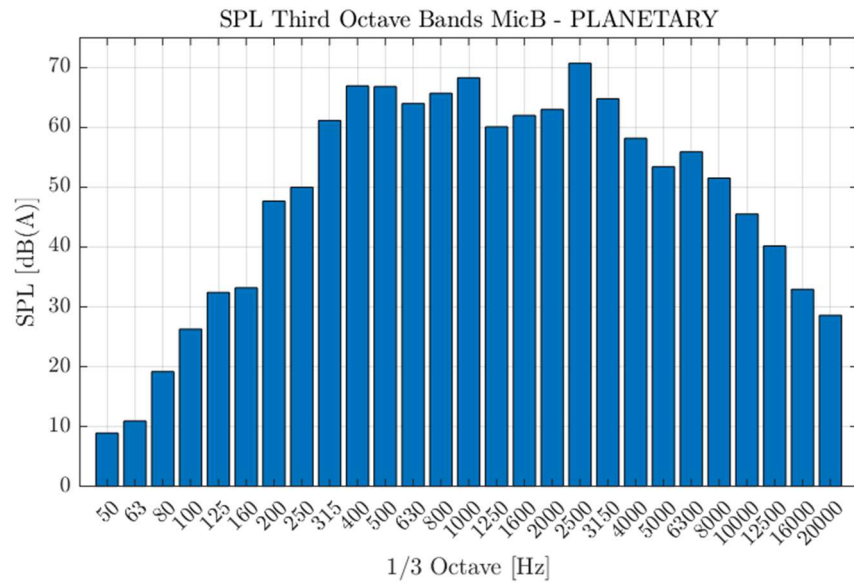


Figure 34 – Third Octave bands microphone B

This is a typical representation for the noise analysis. This plot will be compared with the same obtained from the cycloidal prototype. In this way, it is possible to understand if different frequency ranges will be excited.

- **Regenerative mode**

The analysis conducted for the active mode is also replicated for the regenerative mode.

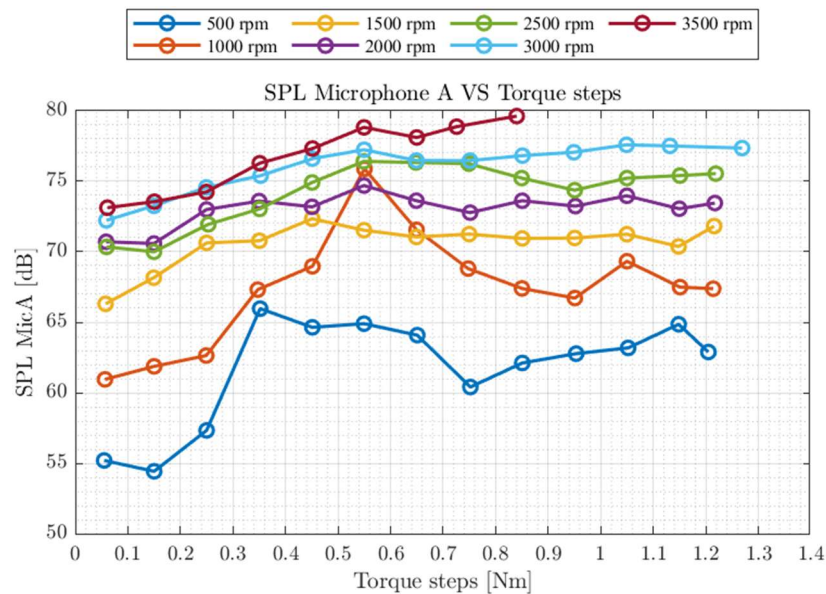


Figure 35 – SPL microphone A vs torque steps

2. Experimental analysis: planetary vs cycloidal RRSA

In regenerative mode the test bench configuration has presented some issues, as Figure 35 shown. In fact, the test bench had significant limitations in drive torque because the counter-motor had to overcome the load of the RRSA and all the other frictional forces. As it is possible to see, it was not possible to complete the test procedure explained in paragraph 2.2. However, similar considerations can be drawn: the pattern for all the speed cases is pretty similar.

In the following figure an acoustic performance map is described.

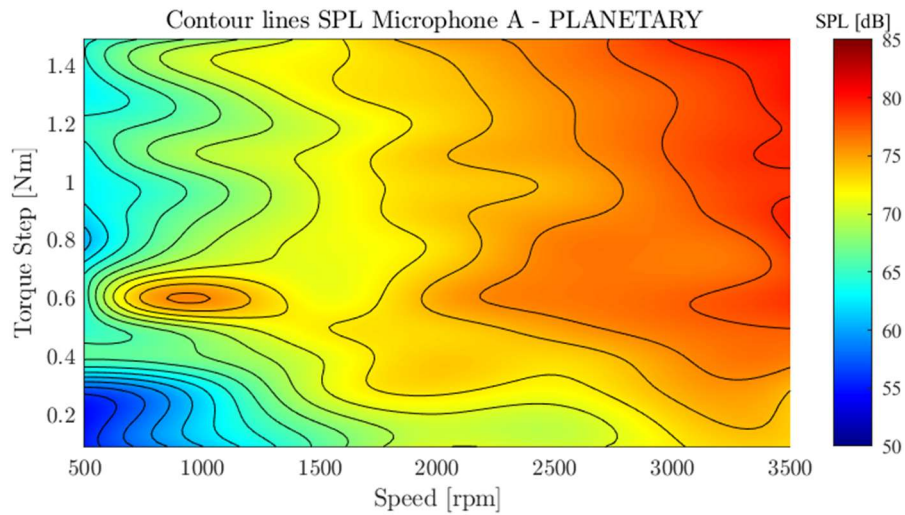


Figure 36 – Contour lines SPL microphone A

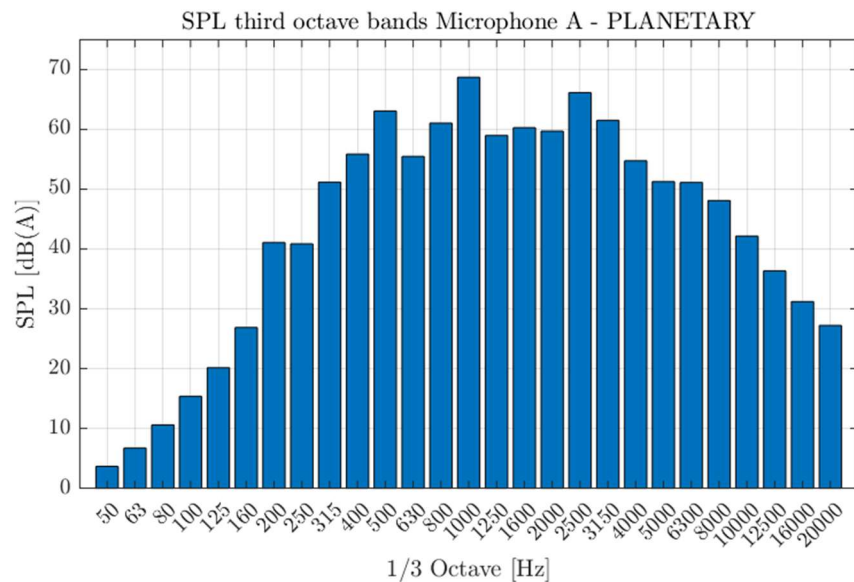


Figure 37 – SPL third octave bands microphone A in regenerative mode

2. Experimental analysis: planetary vs cycloidal RRSA

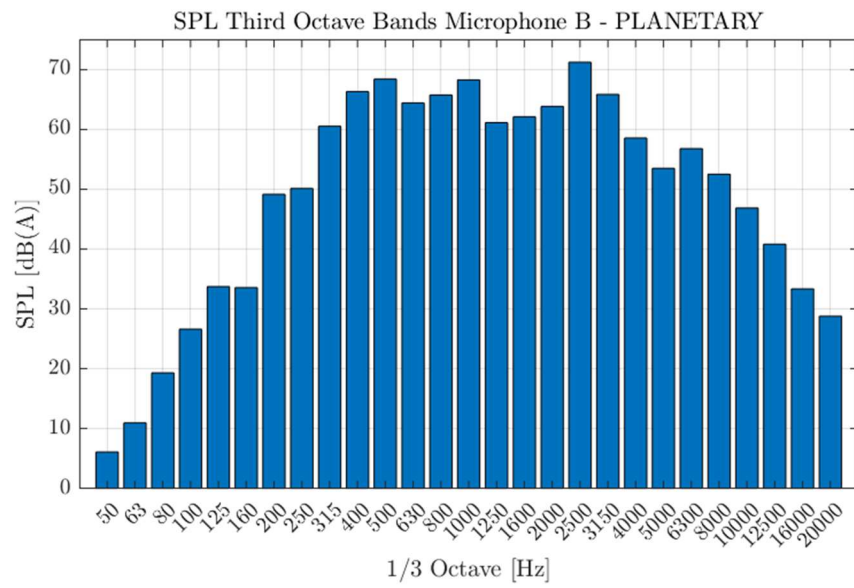


Figure 38 – SPL third octave bands microphone B in regenerative mode

The typical frequency analysis using third-octave bands is presented for both microphones.

2.3.2 Cycloidal prototype results

The same procedure is repeated, substituting the planetary reducer with the new cycloidal prototype. The NVH data coming from the SCADAS LMS III, are also postprocessed in the same way.

2.3.2.1 Cycloidal vibrational analysis

Starting from the excitations generated by the housing, a fast Fourier transform is performed. Here below the results are reported.

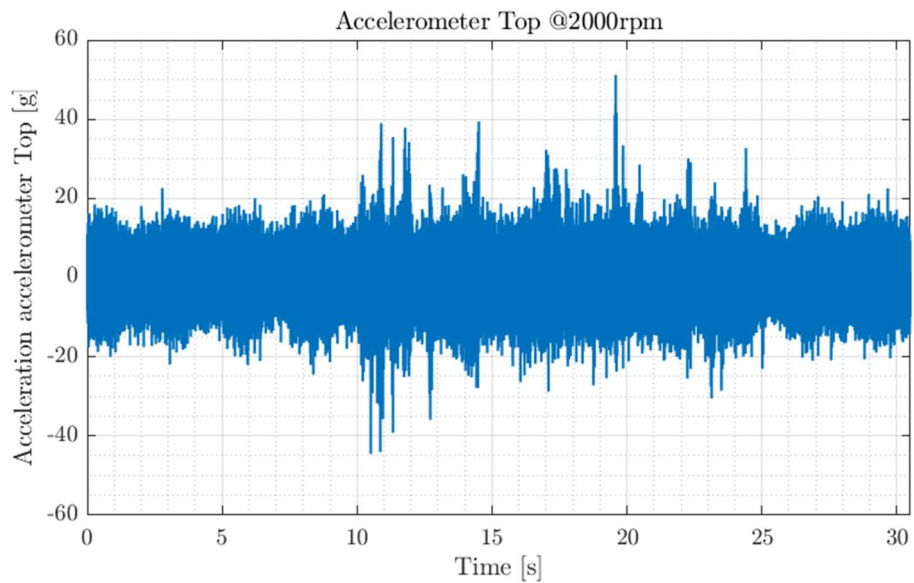


Figure 39 – Accelerometer Top raw data in time domain

The FFT is reported, too.

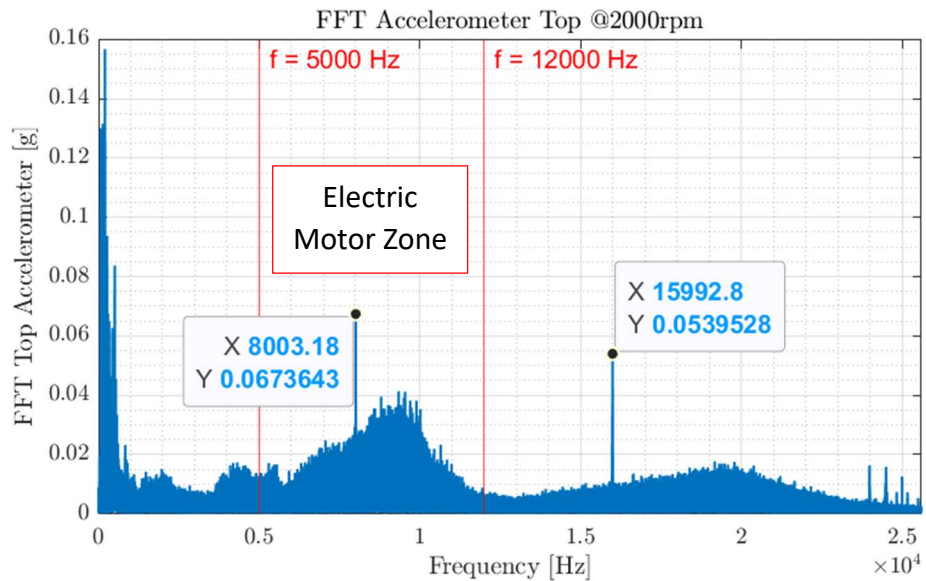


Figure 40 – FFT of the complete test at 2000 rpm

2. Experimental analysis: planetary vs cycloidal RRSA

In the same way of the planetary prototype, it is possible to divide the spectrum in two macro-zone:

1. Excitations related to the mechanical part: frequency range from 0 Hz to 1500-2000 Hz
2. Excitations related to the electrical part: frequency range from 5000 Hz to 12000 Hz.

In Figure 40 some peaks are also visible around 8000, 16000 and 24000 Hz, which as explained for the planetary prototype, they are not related to the prototype itself. These peaks represent the first, the second and the third harmonic of a vibration emitted by the inverter fan.

Move on a more in-depth analysis of the first zone: 0-1500 Hz. This is the frequency range of interest for the goal of this comparison. For an accurate comparison, the frequency range of 0-1500 Hz was analysed using data from a region where torque is exerted by the RRSA, consistent with the approach used for the planetary prototype. Here below the FFT spectrum is reported.

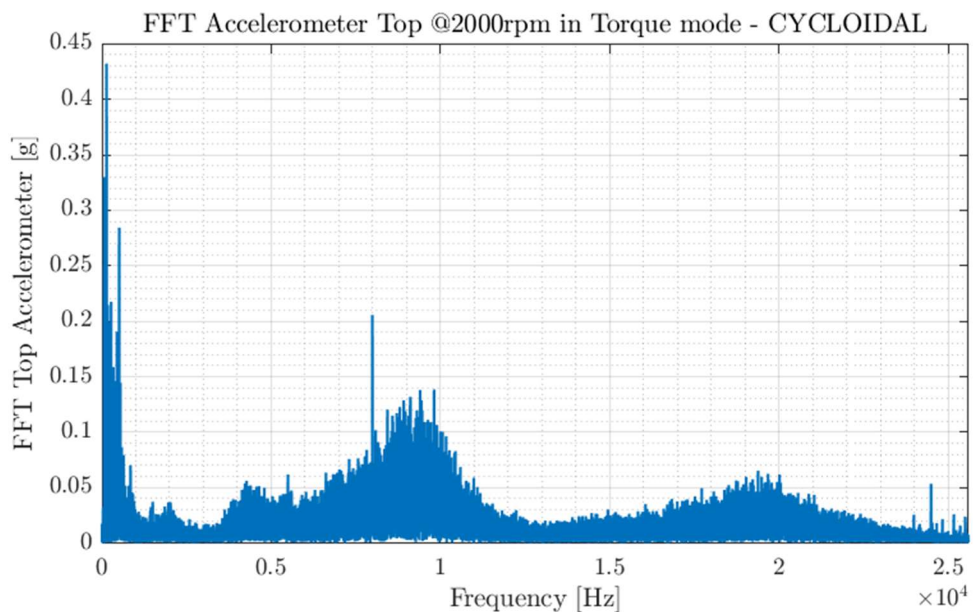


Figure 41 – FFT spectrum whit RRSA in torque mode

The main difference between the figure 40 and the figure 41 is the maximum value of the spectrum. The first one has a maximum value of 0.15g, the second one of 0.44g. In Figure 42 a focus on the frequency range of 0-1500 Hz is reported.

2. Experimental analysis: planetary vs cycloidal RRSA

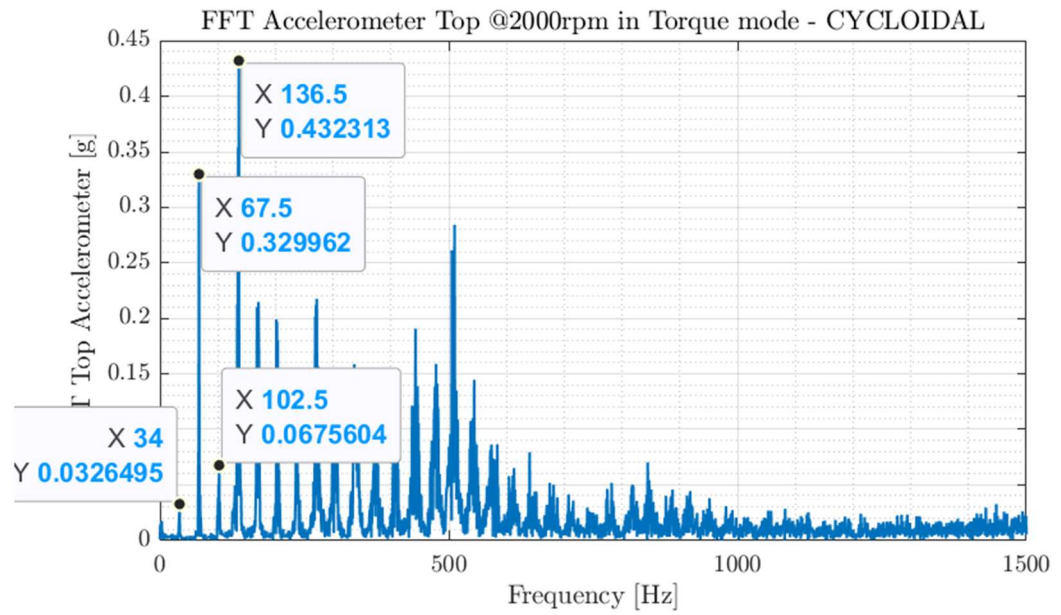


Figure 42 – FFT spectrum in the frequency range 0-1500 Hz

In Figure 42 several equidistant peaks can be seen. As shown in Table 6, the rotational frequency of the rotor shaft, which rotate at 2000 rpm, is equal to 33.3 Hz. In this figure the first peaks value is highlighted. These peaks represent all the rotational harmonics of the rotor shaft.

	1 st harmonic	2 nd harmonic	3 rd harmonic	4 th harmonic	5 th harmonic	6 th harmonic
Calculated	34 Hz	67.5 Hz	102.5 Hz	136.5 Hz	170.5 Hz	202.5 Hz
Measured	33.3 Hz	66.6 Hz	99.9 Hz	133.2 Hz	166.5 Hz	199.8 Hz

Table 7 – Calculated vs measured harmonics

Obviously, it is possible to affirm this, besides the number, because this analysis has been conducted for all the cases. For this reason, a waterfall plot is here reported.

2. Experimental analysis: planetary vs cycloidal RRSA

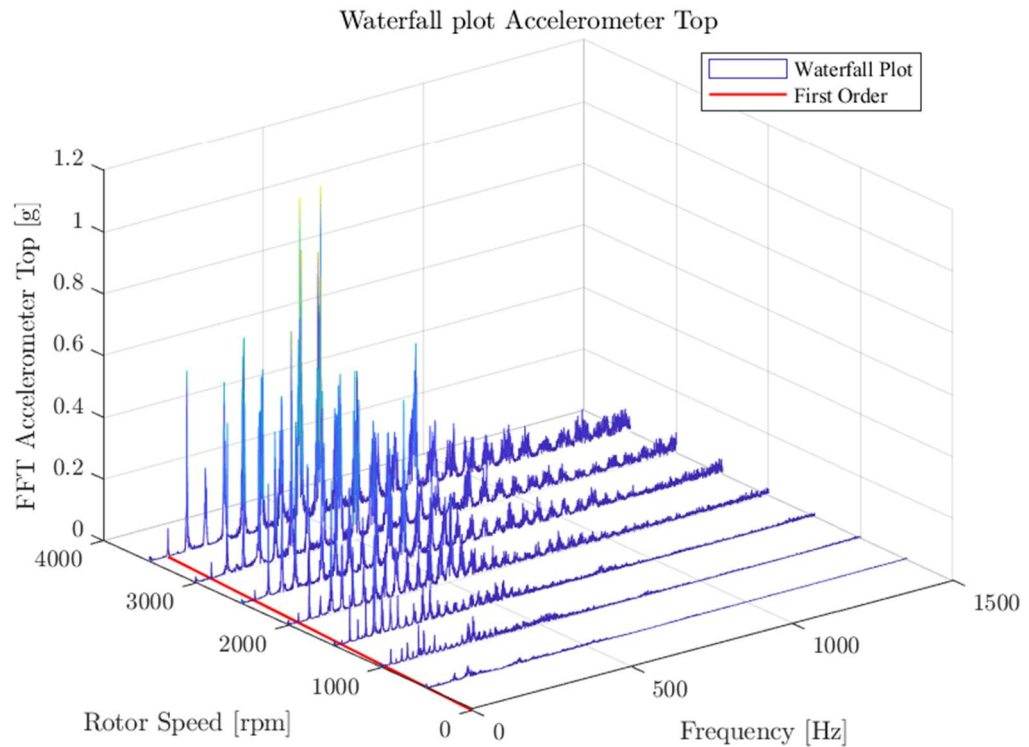


Figure 43 – Waterfall plot cycloidal prototype

In Figure 43, equidistant peaks are visible across all the studied cases, representing the harmonics of the rotor shaft. The red line represents the first-order harmonic of the rotor shaft. Another important feature is the observed pattern in the harmonic behaviour. The harmonics are significantly amplified in the 0-250 Hz frequency range, after which they become smoother. A second amplification occurs around 500 Hz, followed by a reduction in harmonic amplification beyond that frequency. Notably, in all cases except for the final one (3500 rpm), the harmonics show less amplification in the higher frequency range. What is possible to say is that there is something in those frequency ranges able to amplify the rotor harmonics, maybe as explained in Paragraph 2.1.1, this behaviour could depend on the response of the testbench.

2.3.2.2 Cycloidal acoustic analysis

- **Active mode**

Having completed the vibrational analysis, it's possible to move on the acoustic analysis. Starting from the pressure acquired from the microphones during the tests, a complete acoustic analysis in order to obtain the sound pressure level is conducted.

2. Experimental analysis: planetary vs cycloidal RRSA

Here below the first plot is reported.

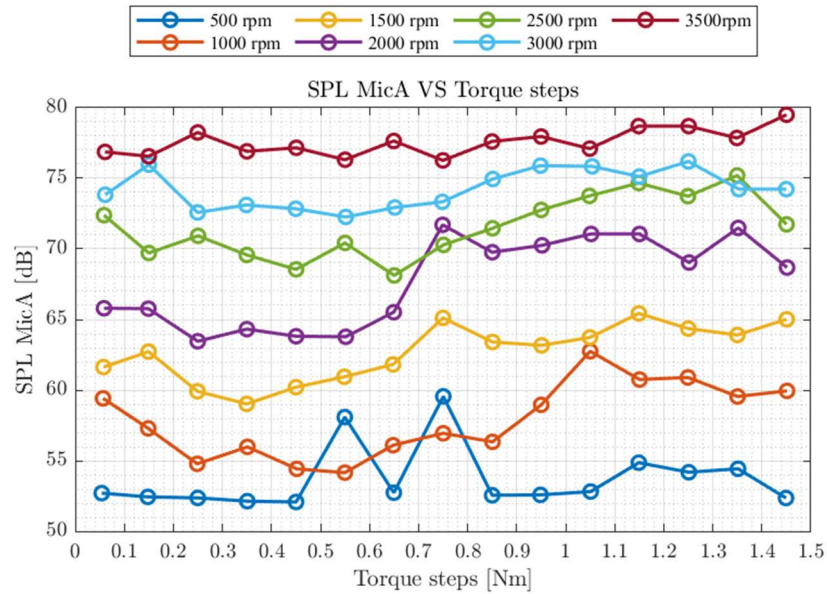


Figure 44 – SPL Microphone A in dB

In Figure 44, it is possible to see a similar pattern among all the speeds. There is a small rise of decibel when the torque goes up. Actually, the pattern is almost flat and this indicates a larger dependency from speed, apart from the first case where the limitations of the test bench led to a trend that is less consistent with the other cases. The post-processing procedure to obtain the Figure 44 is the same of the planetary prototype.

A further representation of the acoustic results obtained is introduced.

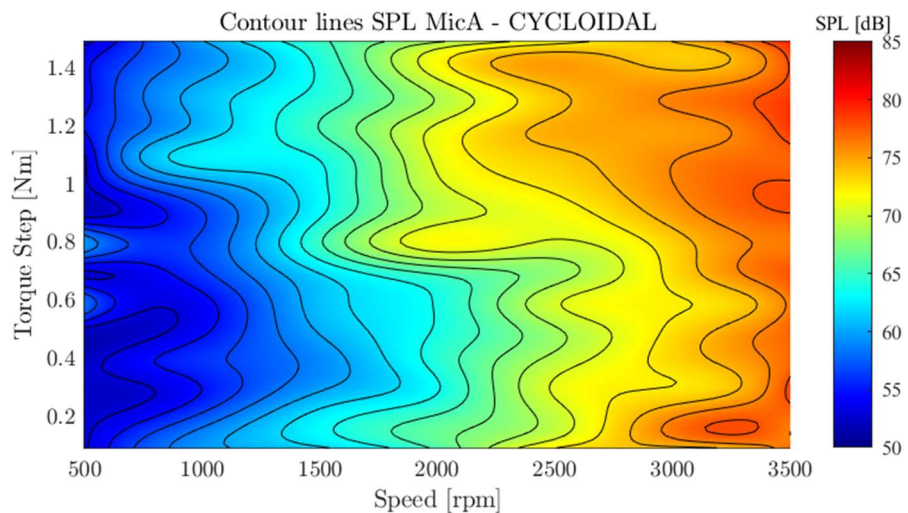


Figure 45 – Contour lines of the microphone A

2. Experimental analysis: planetary vs cycloidal RRSA

This is a contour lines plot. The aim of this plot is to represent an acoustic performance map in order to understand in which speed and torque range there are the worst results. The post-processing procedure is the same used for the planetary prototype.

The plots of the third octave bands for both the microphones are here below reported.

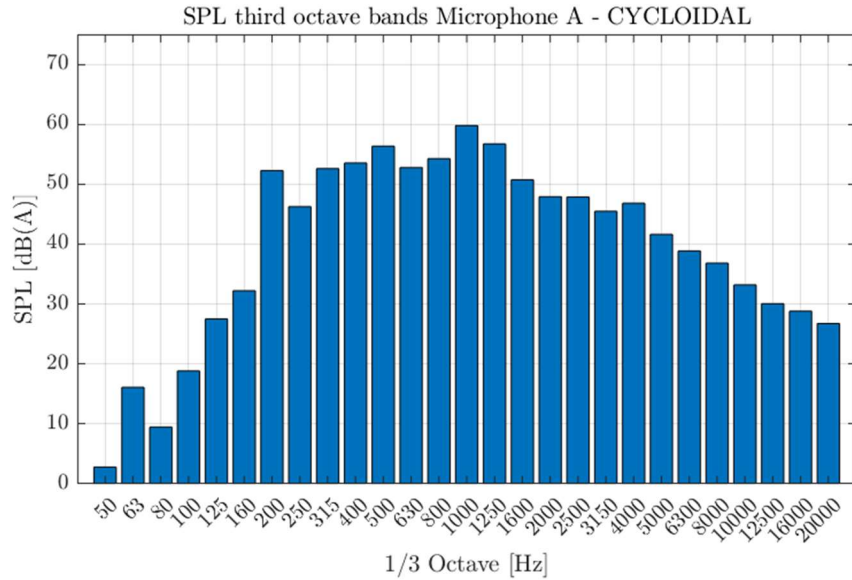


Figure 46 – Third octave bands of the microphone A

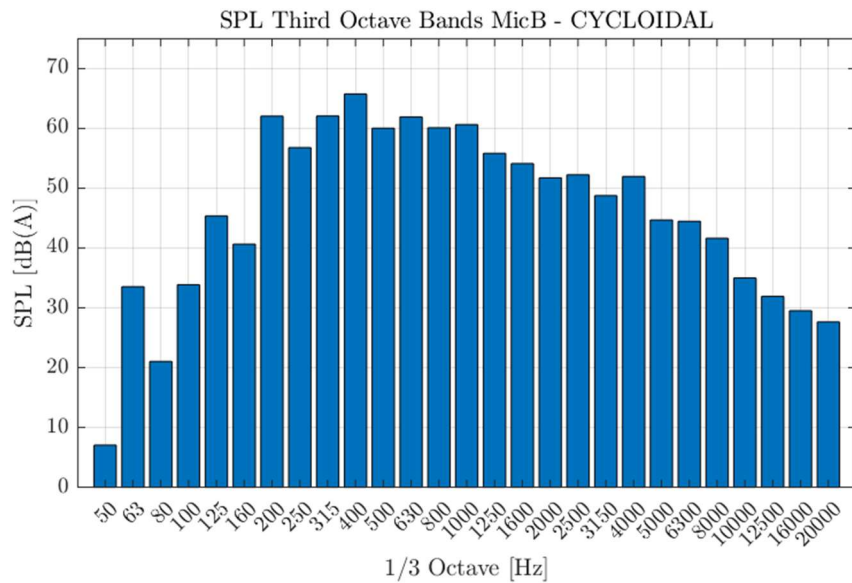


Figure 47 - Third octave bands of the microphone B

The third octave bands representation is typical of the acoustic analysis.

2. Experimental analysis: planetary vs cycloidal RRSA

- **Regenerative mode**

The plots previously generated for the active mode are also recreated for the regenerative mode. In the next section, a comparison between the active and the regenerative mode, as well as between the two prototypes will be presented further on.

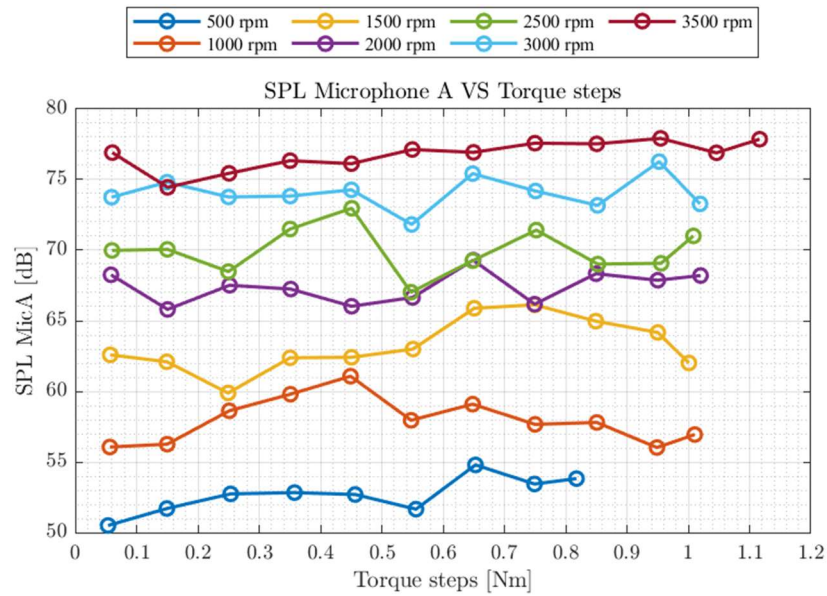


Figure 48 – SPL microphone A vs torque steps

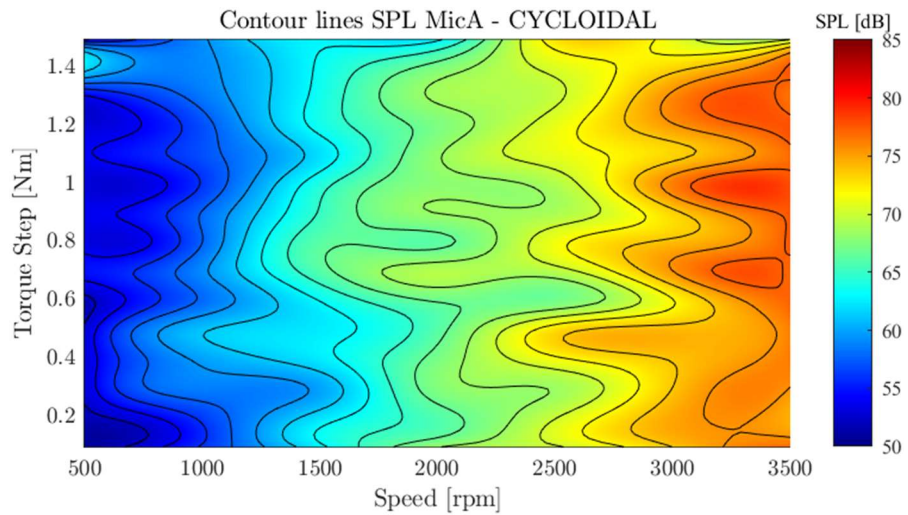


Figure 49 – Contour lines SPL microphone A

2. Experimental analysis: planetary vs cycloidal RRSA

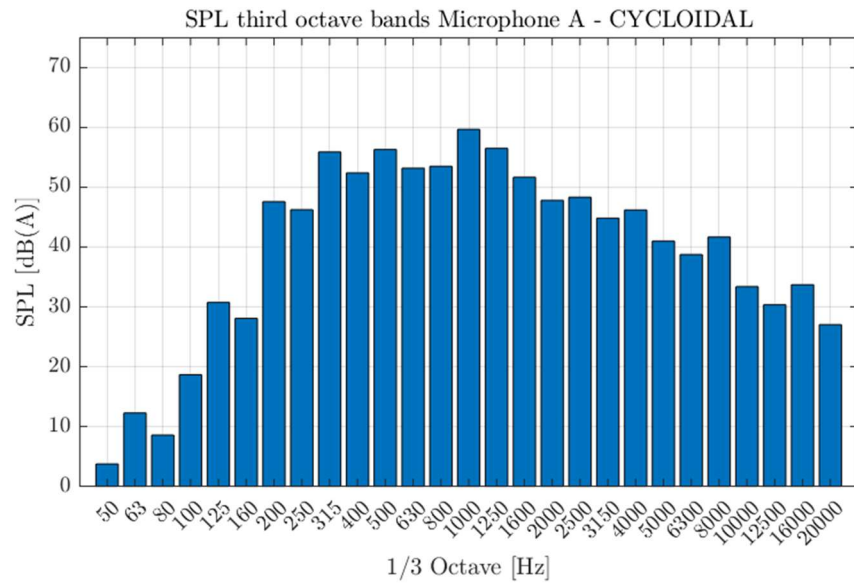


Figure 50 – SPL third octave bands for microphone A

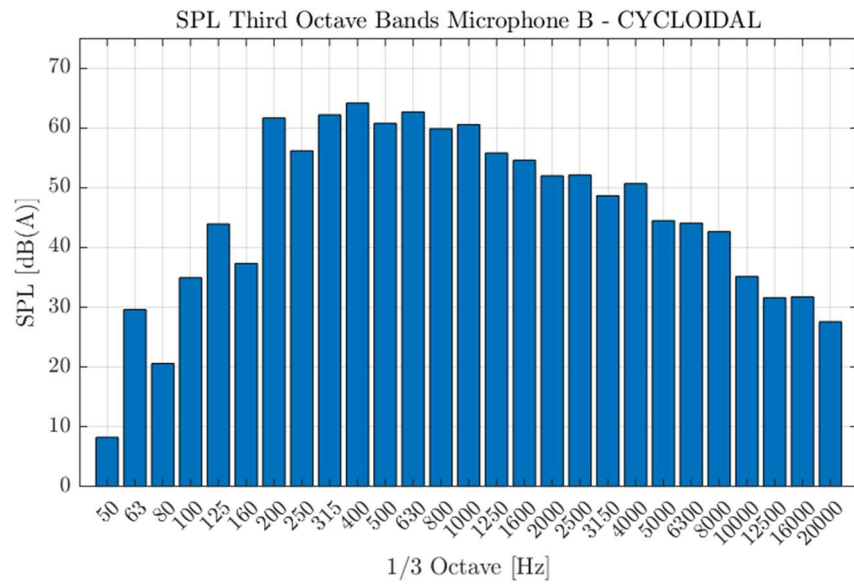


Figure 51 – SPL third octave bands for microphone B

2.3.3 Results overview and prototypes comparison

From the vibrational analysis, the key observation is the maximum value reached in the frequency domain. The cycloidal prototype shows a spectrum with lower value respect to the planetary one. Figure 52 shows both the prototypes in frequency domain so that the differences can be better seen.

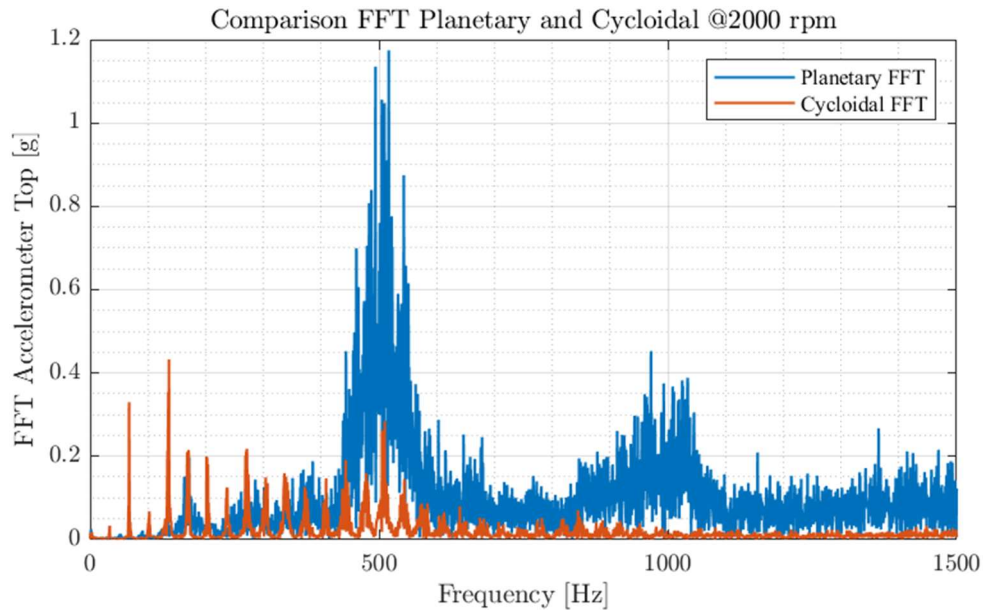


Figure 52 – FFT 0-1500 Hz comparison

In the frequency range between 0 Hz and 1500 Hz, as shown in the Figure 52, the maximum values are:

- 1.175g for the planetary prototype
- 0.432g for the cycloidal prototype

This indicates a reduction of around 65% in structural excitations for the cycloidal prototype. However, it is important to say that it does not mean that the cycloidal prototype will be automatically less noisy, but this is a good starting point. Lower peak values in the spectrum could still result in significant noise if the excitations are spread across a wider frequency range.

For this reason, the acoustic analysis has been conducted, too. The first thing to highlight is that the acoustic results must not be taken as absolute values. The test has not been performed in an anechoic room, but in a laboratory (see figure 17) with all the issues of background and reverberation noise. Obviously, the test was carried out under the best available conditions, i.e. isolating the workplace as much as possible. As said, the aim of this test campaign was to

2. Experimental analysis: planetary vs cycloidal RRSA

make a comparison between two different prototypes. For this reason, the configuration used for the above test campaign was considered acceptable.

The acoustic results can be divided in two different sections:

1. The comparison between active and regenerative mode for each prototype
2. The comparison between the planetary and cycloidal prototypes.

2.3.3.1 *Active vs Regenerative mode*

The planetary prototype, as shown in Figure 31, in active mode at the maximum speed (3500 rpm) and at the maximum torque (1.5 Nm), the SPL reached about 82 dB. In regenerative mode (see Figure 35), due to the issues with the test bench, the SPL peaked at 79.5 dB. This value is obtained at the same speed, but the maximum torque delivered was of 0.85 Nm. At the same speed and torque, the value of the SPL is practically identical. This suggest that the results in terms of maximum values are the same. In order to understand if the results are equal for all the speeds, it is useful to compare the Figure 32 and 36. In these figures the pattern is very similar, so it is possible to affirm that in both modes the SPLs reach the same values.

The same analysis can be carried out for the cycloidal prototype. In active mode (Figure 44), the maximum SPL is around 79 dB. In regenerative mode (Figure 48), the maximum SPL is around 77 dB. For the same issues listed above, in regenerative mode the maximum value is reached at 3500 rpm but at torque value of 1.1 Nm. Comparing Figures 44 and 48, the SPL values at 3500 rpm and 1.1 Nm are nearly identical. For this reason, a further comparison of the contour plot in the figure 45 and 49 shows similar pattern, but the active mode displays more intense colours, i.e. higher overall SPL values.

2.3.3.2 Planetary vs Cycloidal Prototype

The main focus of this research is to compare the two different prototypes. As seen in previous paragraph, there are not so many differences in active and regenerative mode for both the prototypes. For this reason, the comparison in this paragraph is conducted in active mode only. The difference in the peak SPL for the maximum speed is small, only 3-4 dB. For this reason, it is useful to compare the contour plots.

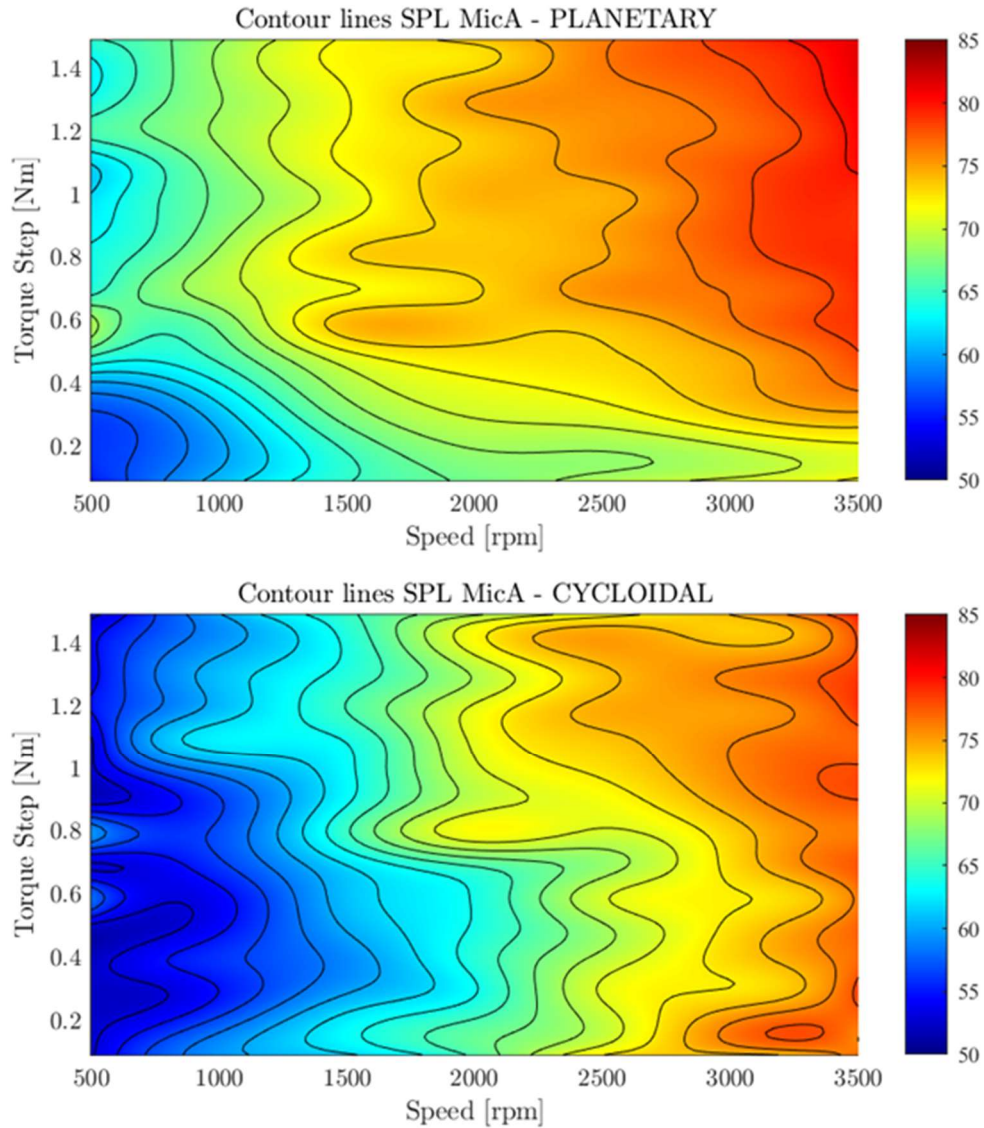


Figure 53 – Contour plot comparison

In Figure 53 it is possible to see that the cycloidal prototype shows lower SPLs across all speed steps confirming a significant noise reduction. In addition, it is possible to notice different behaviour between cycloidal and planetary

2. Experimental analysis: planetary vs cycloidal RRSA

prototype. The cycloidal prototype shows a pattern that is almost solely dependent on speed, unlike the planetary prototype.

To better highlight the acoustic improvements achieved with the cycloidal prototype, the “delta acoustic performance map” is reported. It is obtained as follows:

$$\text{delta acoustic performance map} = SPL_{\text{planetary}} - SPL_{\text{cycloidal}}$$

In this way, the positive results correspond to superior acoustic performance of the cycloidal prototype respect to the planetary one.

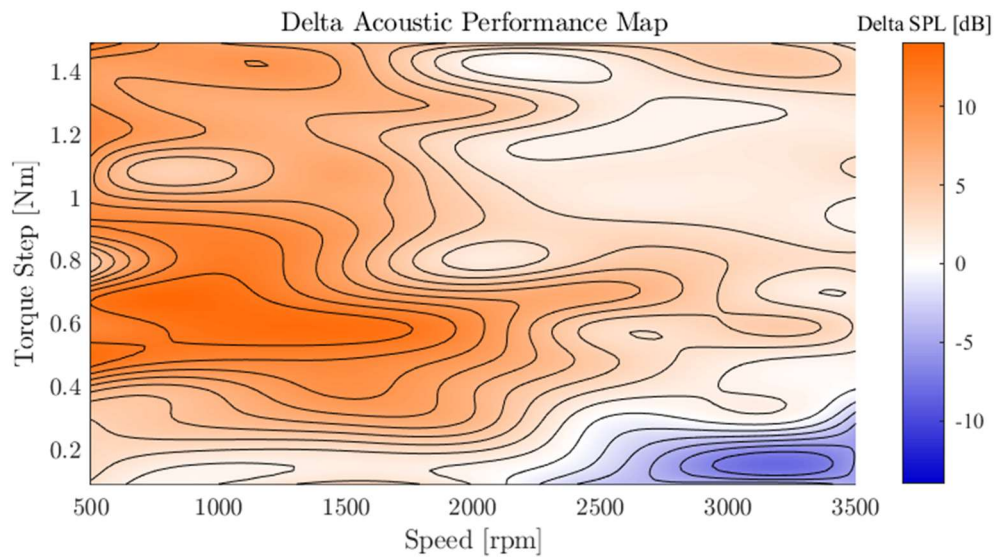


Figure 54 – Delta acoustic performance map

In Figure 54, the orange-coloured part is the widest. It represents the areas where the cycloidal prototype performs better than the planetary one. The white part represents the areas where the prototypes show similar performance, instead. There is only a small part (the blue-shaded) where the planetary prototype performs better than the cycloidal one. It is important to highlight that the cycloidal prototype even shows a noise reduction of 14 dB (the brightest orange-coloured area).

To make a complete analysis it is possible to compare the third octave bands for both the prototype, which provide insight into the most affected frequency ranges. Hence, it is useful to compare the third octaves bands.

2. Experimental analysis: planetary vs cycloidal RRSA

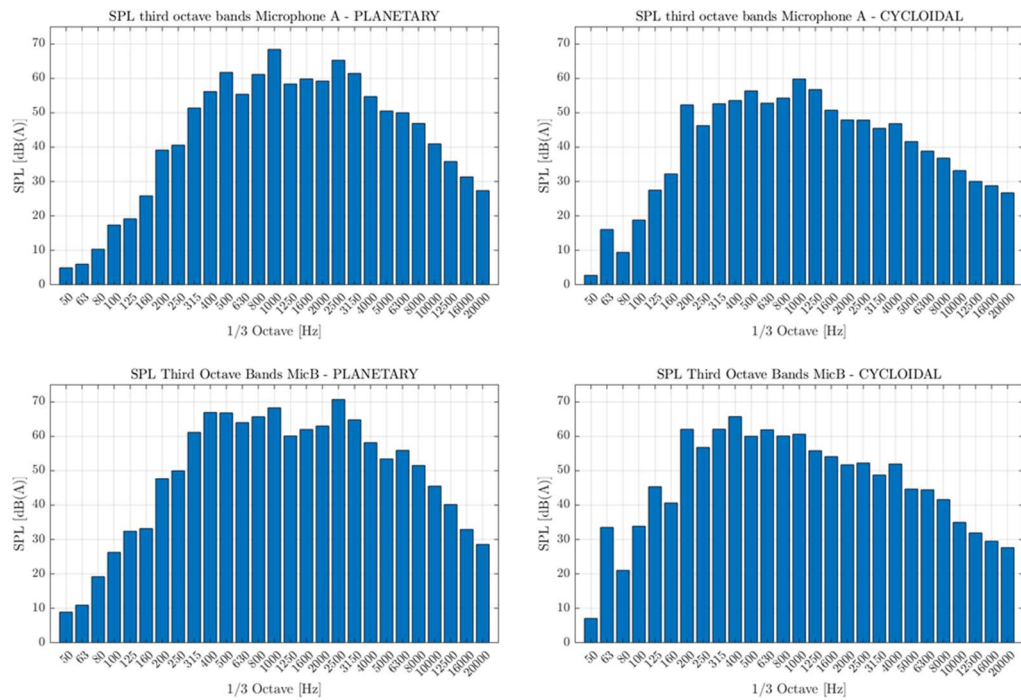


Figure 55 – Third Octave Bands comparison

In figure 55 it is possible to see that the cycloidal prototype generates higher noises in a lower frequency range. In addition, the maximum values are around 8-9 dB(A) lower.

In parallel with these acoustic tests, efficiency measurements were also conducted. The planetary prototype shows a higher efficiency respect to the cycloidal one. In particular, the max efficiency of the planetary prototype is 72 % in active mode and 66 % in regenerative mode; the cycloidal max efficiency is 57 % in active mode and 38% in regenerative mode.

In the following pictures, the design geometry differences between the two prototypes are shown.

2. Experimental analysis: planetary vs cycloidal RRSA

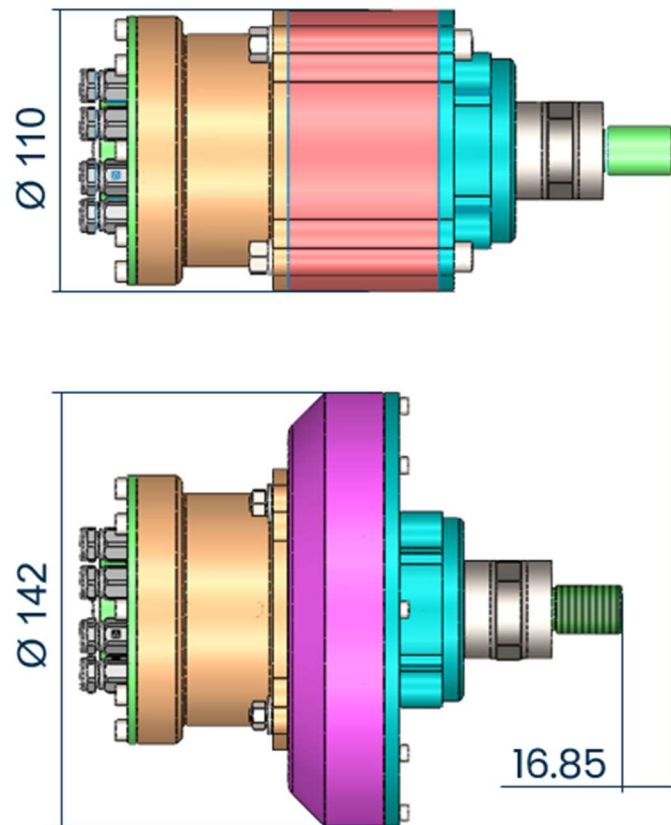


Figure 56 – Planetary and cycloidal geometry differences [22]

All these considerations can be summarized in the Table 8.

Prototype	Mode	Max noise [dB]	Frequency range [Hz]	SPLs ≤ 65 dB [%]	Max efficiency [%]	Axial size [mm]	Radial size [mm]
Planetary	Active	82	400-4000	11.28	72%	193.95	110
	Regen	79.5			66%		
Cycloidal	Active	78	200-1600	42.52	57%	177.1	142
	Regen	77			38%		

Table 8 – Summarize results table

3 Simulation analysis

In recent years, the role of the NVH in vehicle design has become increasingly important. Just as simulative techniques have increasingly become the leading players in design, simulation in NVH field has also become a widespread practice. In this way, modifications and improvements can be made at an early stage of design. In the first Chapter, the Transfer Path Analysis (TPA) has been introduced. The use of simulation methods, led to its natural evolution: Vehicle Interior Noise Simulation (VINS) by FEV® [28-29]. This methodology combines all the features of the TPA with a real simulation part through CAE (Computer-Aided Engineering) tools. An overview of the main simulation methods will be presented in the next section.

3.1 Simulation methodologies in automotive industry

Nowadays a lot of methodologies are available for the simulation of the interior vehicle noise. Here below a short description of the most popular is reported.

3.1.1 Finite element method (FEM)

The finite element method is one of the most popular methods in the automotive industry. For the noise refinement, this method is highly recommended for the evaluation of the structural borne excitations. It, in fact, has a good correlation for the low frequency range. It requires that all the surfaces and objects, both the solid structure and the fluid cavities, be properly modelled. In this way, a fully coupled solution between the vibrations of the structured accelerations and the pressure level of the cavities will be obtained [14]. Here below an example is reported.

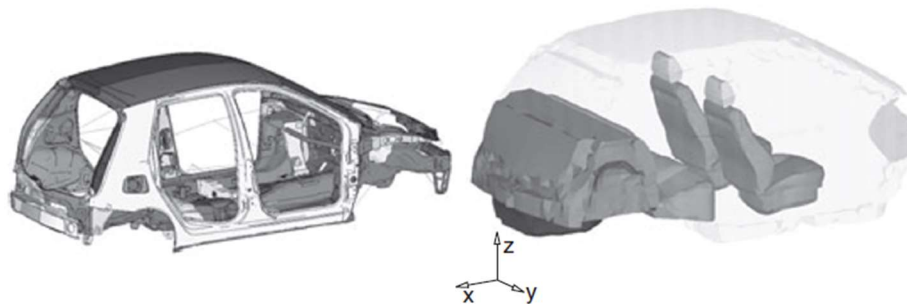


Figure 57 – FEM of a car's structure and acoustic cavity [14]

3.1.2 Boundary element method (BEM)

The boundary element method is less known in the structural simulation environment, but in the acoustic field has an important role. It is developed in the late 1970s. The main difference between FEM and BEM lies in the way the domain is discretized. Both methods discretize the domain in element, but the first one discretizes all the structures, instead the latter discretizes only the boundaries between two bodies. This allows to reduce the problem complexity by one dimension.

The BEM theory is based on the solution of the Helmholtz equations. This is time consuming and for this reason it is a method not suitable for simulations in very high frequencies, as they require more and more elements.

Usually, the FEM and the BEM are used simultaneously [30]. Here below a scheme is proposed.

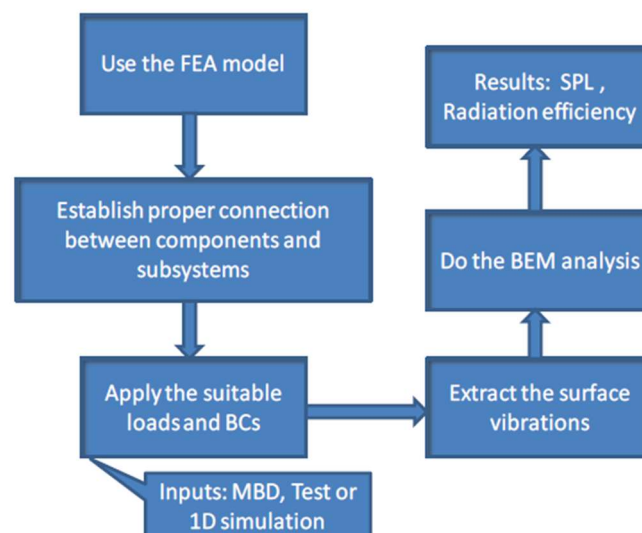


Figure 58 - Steps used for FEM and BEM analysis [30]

3.1.3 Infinite element method (IEM)

The infinite element method is the natural evolution of the BEM. As said, the main drawback of the BEM is that it is very time consuming. This new method is not based on the boundary representation but on the domain representation. It means that the domain-based method will not look for the exact solution, but it will try to approximate its solution within a finite region close to the radiating body. To do this, the volume around the radiating body will be discretized through finite elements (FEM) and the acoustic pressure will be obtained at each element node [14].

The application field of the IEM is the same of the BEM one. It is very useful for low and medium frequencies.

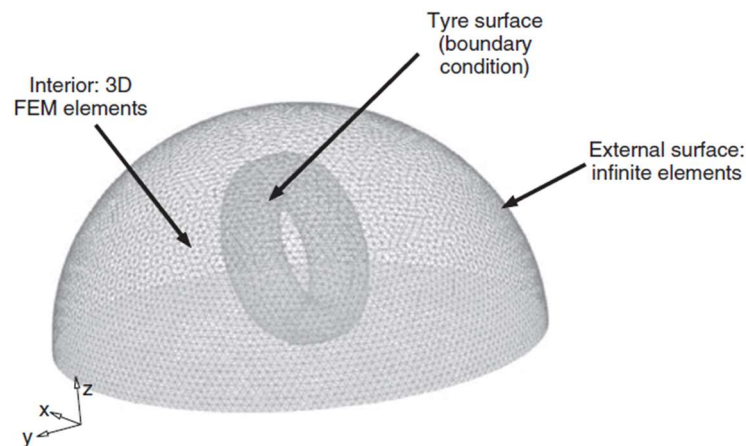


Figure 59 – Infinite element model of a car's wheel [14]

3.1.4 Statistical energy analysis (SEA)

The statistical energy analysis is one of the last born in the simulation methodologies. It allows to overcome the limitations of the previous methodologies. So, it is possible to obtain good results for the high frequency range. It is the recommended method to study the airborne excitations.

The idea behind this method is completely different. In SEA, the vibroacoustic problem is linked to an equivalent thermal or electrical analogue one in which the vibroacoustic energy is related to temperature or voltage [14]. In this way, it will be much less time consuming, so it is very useful in the first steps of design.

The application of this method requires a lot of experience. Furthermore, it requires many parameters, which are sometimes difficult to be obtained.

3.2 Simulation environment

The use of a simulation model allows various modifications to be made to the original model in order to achieve some improvements. For this reason, it was decided to recreate the RRSA in its epicyclic version with spur gears. To do this, it was decided to use the platform made available by AVL®: Excite M.

3.2.1 AVL® Excite M

AVL® is a leader in the field of engine development thanks to all the experience gained over the years. AVL® Excite is a powerful tool for the NVH and durability simulations of powertrain and drivelines.

AVL® Excite M is a package which allow to model and simulate the dynamic, NVH, durability and efficiency of drive units. It is possible to build simple model using rigid default components; otherwise, it is possible to recreate more sophisticated models, associating to these defaults components, real bodies with correct geometry, stiffness, mass and as a result complex flexible structure. Dynamic calculations could be carried out both in the time domain and in frequency domain [31].

- **Workflow**

The model design starts with the “predefined bodies”, such as shafts and gear wheels, found in the “component pane”. Excite M environment also provides different assemblies such as “Planetary Gearset”. The second step is to connect the bodies through different types of joints. To conclude this first stage, the kinematic and/or kinetic boundary conditions, such as predefined motion and loads, must be applied.

After this first stage, the baseline model can undergo the first simulation, in order to understand if it performs correctly. In the following section a schematic way to obtain the model with real bodies will be reported.

Hence, the next step is to bring the model more in line with reality. To do this, it is necessary to insert the real geometries and the real physical properties (inertia, stiffness and damping) of the components. All these properties will be transferred into Excite M environment through files with *exb extension. Since Excite M does not present a mesh tool, these files will be generated with the help of Ansys® Workbench. The main steps to obtain these types of files are:

1. Creation of *cdb file, which contains the mesh information. It is realized into the Ansys® WB environment through the “Static Structural” block.
2. Importing this file inside the Excite M’s app: “Component Modeler”.
3. Making the “Condensation task”: in this phase all the mesh nodes selected will be “condensed” into a single “Excite body node”. In this way all the information of the selected mesh nodes will be transferred to the “Excite body node”.
4. The condensation task will generate three different files (*fea, *inp, *cdb extension) that are useful for the creation of the *exb file, since they include all the commands and options for the creation of the *exb file.
5. Within the Ansys® WB environment, using the “Modal” block, it is now possible to perform the last step and make the *exb file.

6. Finally, the *.exb file is ready to be inserted in the Excite environment.



Figure 60 – Creation sequence of *.exb file: the steps to do with the help of Ansys® WB are the orange blocks; the step to do inside the Excite M environment are the blue blocks.

An example showing the starting and ending point of the *.exb creation process is given here.

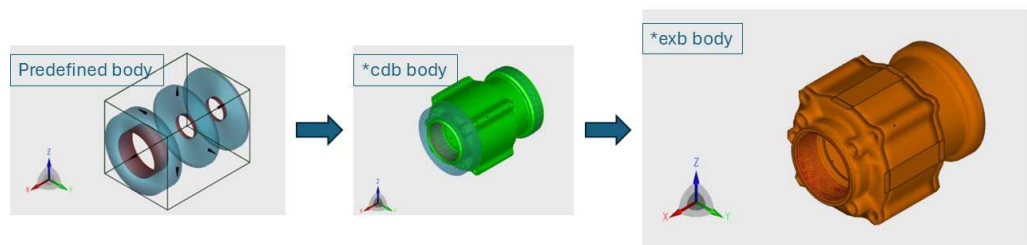


Figure 61 – Step to obtain *.exb bodies.

3.2.2 RRSA Planetary prototype in Excite M

Repeating the procedure described above for every single body, it is possible to obtain the model with all the inertia, stiffness and damping contribution.

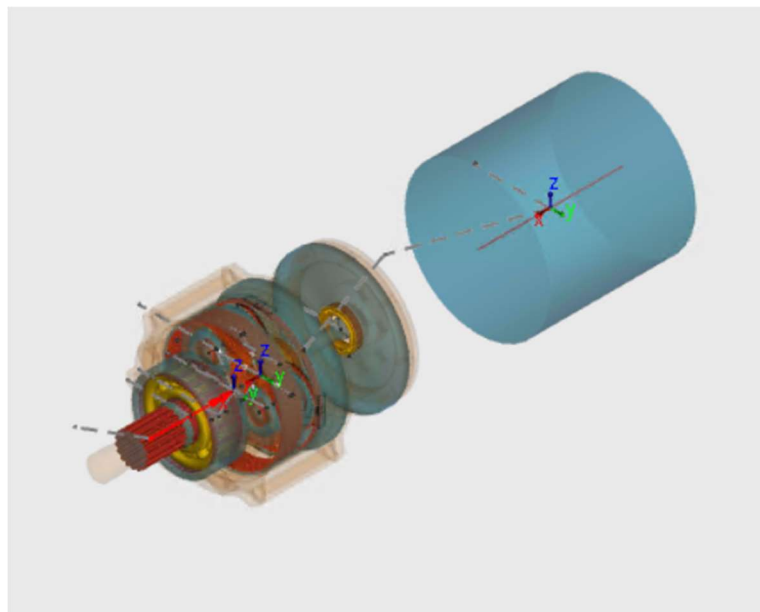


Figure 62 – RRSA Planetary prototype in Excite M

In Figure 62, in addition to the prototype, it is possible to see a blue shaded cylinder, the “Kinematic Driver”. This is the substitute of the electric motor. Obviously, it is a simplified configuration, but for the goal of this thesis, it was important to model only the gearbox of the RRSA. To define the power transmitted through the reducer, the following boundary conditions are applied:

- Speed velocity at the “Kinematic Driver”
- Counter-torque applied to the spline (at the lever position).

Having completed the assembly of the model, simulation can start. For this work purposes, the simulation is conducted in time domain. The simulation setting allows several parameters to be changed. After some tuning, the main parameters are:

- Kinematic Driver’s rotation angle: 720 degrees
- Computation settings: variable step size, minimum step size: 1e-9 degrees, maximum step size: 0.05 degrees, initial step size: 1e-4 degrees
- FFT lower bound frequency: 0 Hz
- FFT upper bound frequency: 10000 Hz
- Order extraction for the Campbell diagram: 2 (GMF 2nd stage), 14 (GMF 1st stage), 28 (second harmonic GMF 1st stage)

Simulations were carried out for seven different cases, from 500 rpm to 3500 rpm, in order to replicate the experimental analysis presented in chapter two.

3.2.3 Simulation method used in AVL® software

In Paragraph 3.1 an overview of the most popular methodologies in automotive industry has been done. The AVL® software uses a new approach because, although the FEM and BEM simulations are the most widespread, they possess inherent limitations, i.e. they are very time consuming, and they require special expertise. This new methodology is the “Wave based technique”.

As known, FEM and BEM methods use approximated shape functions to describe the dynamic response variables. On the other hand, the Trefftz method, from which the Wave Based Technique are derived, proposes the use of approximated solutions, which must satisfy the governing differential equations, but do not mandatory satisfy the boundary conditions [31].

3.3 Simulation results

The aim of this simulation is to prepare and optimize the starting model on which developments can then be implemented in order to improve the acoustic performance of the RRSA prototype. Once the model has been prepared as explained in section 3.2 and the simulation has been completed, the dynamic results of the model are analysed. Figure 63 shows the angular speed of the electric rotor.

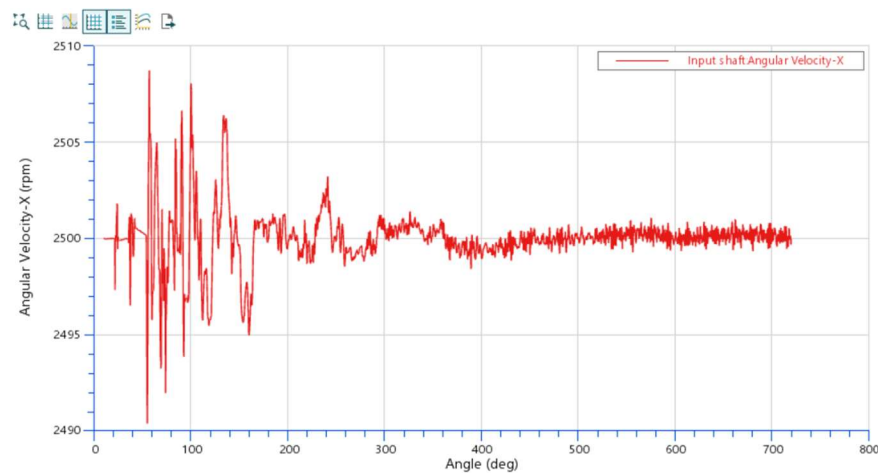


Figure 63 – Rotor angular velocity

In Figure 63 it is possible to see that after an initial transient part, the rotor speed stabilizes itself. The same pattern is possible to see for the 1st stage Carrier angular velocity, shown in Figure 64.

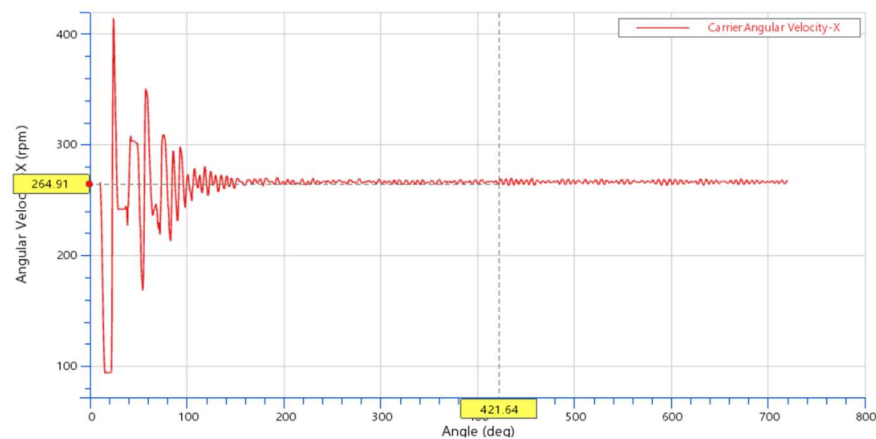


Figure 64 – first stage Carrier angular velocity

The transient part is justified by the number of teeth in contact. Figure 65 shows the number of teeth in contact between the Sun gear and one of the three planets of the first stage.

3. Simulation analysis

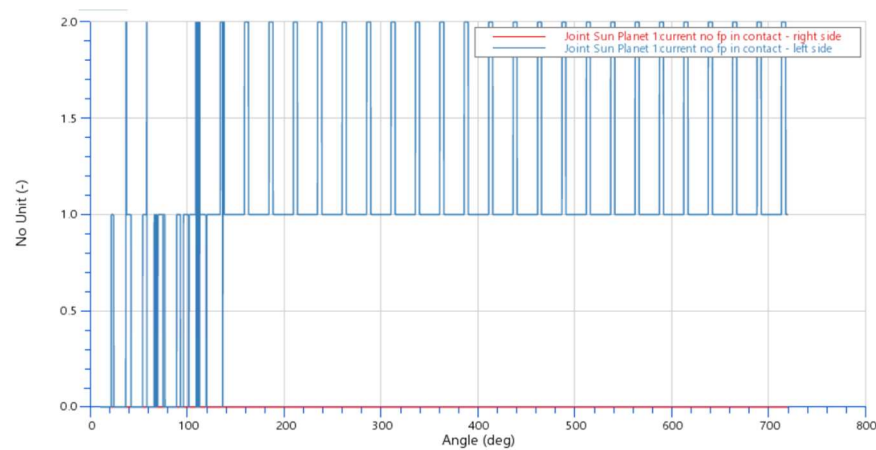


Figure 65 – 1st stage Sun-Planet teeth in contact

Since this is a vibrational analysis of rotating bodies, they can be analysed using the Campbell diagram. In this way it is possible to identify the main forcing frequencies (orders). As explained in Chapter 2, the forcing frequencies of the double stage planetary gearbox are related with the gear meshing. The main orders are 14.28 for the first stage and 1.52 for the second stage. Figure 66 shows the Campbell diagram obtained.

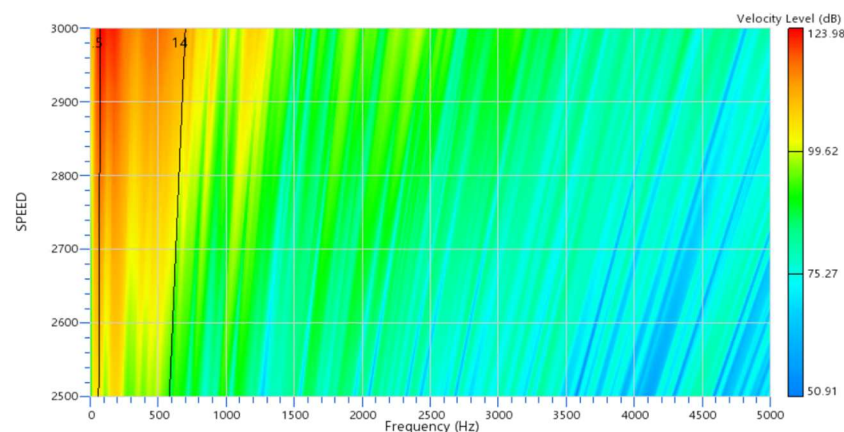


Figure 66 – Campbell diagram and main order lines

In Figure 66, it is possible to see the main excited orders. The higher levels are between order 1.5 and 3. The high-level area extends until order 14. The first important thing to say is that the order lines highlighted in this plot are 1.5 and 14, which are not the ones calculated analytically. This is linked to the *order resolution*. As explained in section 3.2.2, the simulation was run for two revolutions of the “kinematic driver”. The order resolution can be obtained as follows:

$$\text{Order resolution} = \frac{1}{N_{\text{revolutions in results}}}$$

3. Simulation analysis

Consequently, the *order resolution* for two revolutions is 0.5.

As shown in Figure 66, the main order lines excited are related to the first stage and the second stage GMFs. Indeed, it can be interesting to run a new simulation without including the flexible bodies of the first stage, so it does not transmit vibrations to the housing. It is expected that no excited orders will be present around the order 14. Figure 67 shows the Campbell diagram.

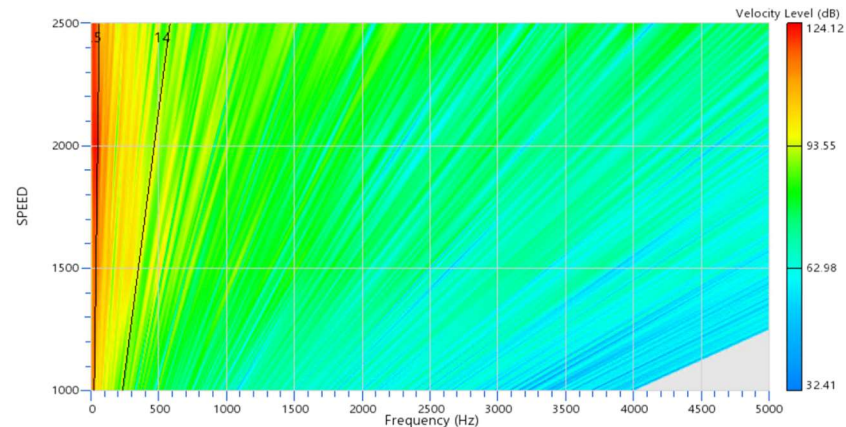


Figure 67 – Campbell diagram with first stage made rigid

Indeed, Figure 67 shows the area around the order 14 no more excited.

The Excite M environment allows to obtain the structural borne contribution.

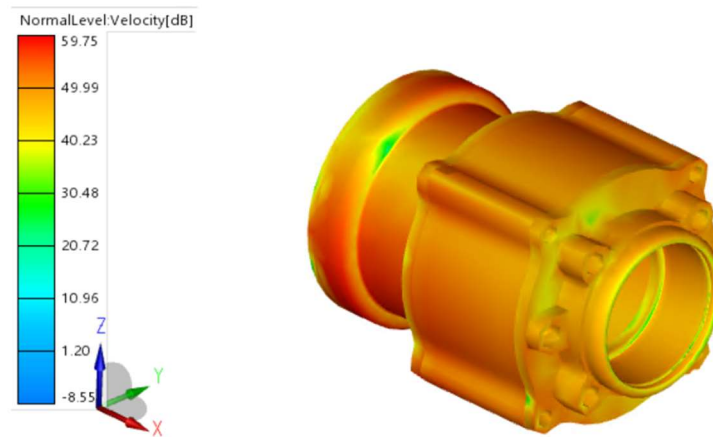


Figure 68 – Housing surface velocity

Figure 68 shows the “Normal level surface velocity” of the Housing. Being a level, it is expressed as dB. To understand if the obtained results have a physical meaning and to partially validate the simulations, it can be useful to analytically compute the Sound Pressure Level (SPL) at one meter distance and to compare it with the results obtained by Galluzzi et al. To do this an approximation has

been done, i.e. the acoustic source has been considered spherical-shaped. A further important approximation is to consider the collision between the particles and the Housing surfaces with no loss. The air atom collision is considered elastic. In this way the mechanical energy is conserved. All these considerations have been done in order to simplify the analytical computation, since the main aim is to estimate the magnitude of the results rather than the exact values, in order to validate the model. The relationship between the acoustic pressure and the particles velocity is described by the so called “Acoustic Ohm law” [27]:

$$p_{acoustic} = \rho * c * v_{particles}$$

where:

- $p_{acoustic}$ is the pressure deviation [Pa].
- ρ is the air density in this case 1.205 Kg/m³.
- c is the acoustic wave velocity propagation in air, in this case equal to 343 m/s.
- $v_{particles}$ is the particles velocity, in this case the results obtained from the simulation [m/s].

The $v_{particles}$ is equal to:

$$v_{particles} = 0.08 * 10^{-3} m/s$$

This is a mean value obtained from the node velocity of the Housing after the transitory part.

Using the Acoustic Ohm law:

$$p_{acoustic} = 0.3361 Pa$$

Applying the definition of Sound Pressure Level (SPL):

$$SPL[dB] = 20 * \log\left(\frac{p_{acoustic}}{p_0}\right) = 84.51 dB$$

The next step is to obtain the SPL at one meter distance. Through the definition of sound power level and according to the inverse proportional law, it is possible to obtain the relationship between the SPL at two different distances. It is described as follow:

$$SPL_2 = SPL_1 + 20 * \log\left(\frac{r_1}{r_2}\right)$$

where:

- SPL_2 is the value at one meter distance.
- SPL_1 is the previous obtained value: 84.51 dB.
- r_2 is equal to 1 m.
- r_1 is the radial size of the RRSA, approximately 0.045 m.

Figure 69 shows the schematic view of the analytical approach.

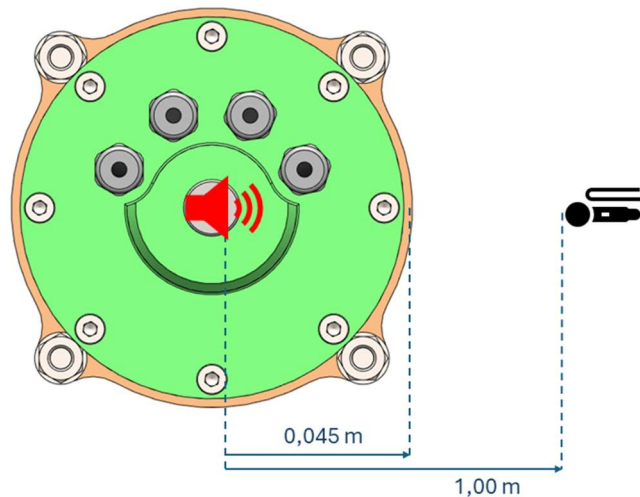


Figure 69 – Analytical approach

Applying the previous equation, the SPL_2 is equal to:

$$SPL_2 = 57.57 \text{ dB}$$

This result has a physical meaning because is not too much far from the results obtained in anechoic room by Galluzzi et al [1]. For a rotor speed of 2500 rpm, Galluzzi et al. reported a sound pressure level of 49.63 dB(A), as shown in Table 4. It is important to highlight that the Galluzzi's tests were carried out without any applied load. In addition, this analytic result is obtained with all the considerations made previously, i.e. no losses and spherical sound source.

Conclusions

Starting from an overview of the suspension system for automotive application, it was possible to see all the advantages and drawbacks of the various employed technologies. Several example of electromagnetic shock absorber were presented and ultimately the prototype under consideration, the Rotary Regenerative Shock Absorber was introduced. Dealing with a NVH analysis, an overview of the main parameters and methods used in this context has been reported. Furthermore, it was possible to see how the noises and vibrations propagate through two distinct paths: structure-borne path and airborne path.

After the state-of-the-art overview, an experimental campaign was carried out, to compare the NVH performances of two RRSA prototypes, equipped with two different speed reducer technologies: planetary and cycloidal. The results lead to consider the cycloidal prototype superior from the acoustic performance point of view respect to the planetary one. In fact, the first shows an SPL inferior to 65 dB for the 42.52% of the tested operational conditions, while the latter achieves the same result only for the 11.28% of them. On the other hand, from the efficiency point of view, the best prototype, both in regenerative and active mode, is the planetary one with a maximum efficiency of 72% (active mode), while the cycloidal speed reducer only reaches 57% (active mode).

Furthermore, a model of the planetary RRSA was created to carry out NVH simulations. These simulations were conducted with Excite M by AVL®. The main goal of this activity is to obtain a baseline model with planetary gearbox and spur gears so that, in the future, it will be possible to introduce some modifications in order to enhance the acoustic performance of the prototype. Being it a CAE tool, it will allow cost and time reduction for the design and NVH evaluation of next RRSA developments. The first obtained results are a good starting point. In fact, they are comparable with those obtained in anechoic room by Galluzzi et al.

There are several improvements that can be implemented, both in experimental and simulative environments. Starting with the experimental setup, the test rig can be improved in order to mitigate the test rig resonances. In this way a more accurate order analysis can be carried out. In addition, these tests can be performed into an anechoic room in order to delete reverberation

and background noise. In this way, the acoustic results could be considered not only for comparison purpose, but also in their absolute values.

The greatest progress, however, can be made thanks to the simulative approach. Several alternatives can be explored for the gearbox realization, starting with the most obvious: planetary gearbox with helicoidal gears. Numerous studies highlight the possible improvements in acoustic performance using helicoidal gears in place of spur gears. In fact, gears with High-Contact Ratio (HCR) show better acoustic performance rather than gears with Low-Contact Ratio (LCR).

A further possible modification to obtain higher acoustic performance is to re-design the Housing. In this way some vibrations at certain frequencies can be eliminated or at least mitigated.

Bibliography

- [1] Galluzzi, R., Circosta, S., Amati, N., & Tonoli, A. (2021). *Rotary regenerative shock absorber for automotive suspensions*. *Mechatronics*, 77, 102580.
- [2] Amati, N., Festini, A., & Tonoli, A. (2011). *Design of electromagnetic shock absorbers for automotive suspensions*. *Vehicle System Dynamics*, 49(12), 1913-1928.
- [3] Savaresi, S. M., Poussot-Vassal, C., Spelta, C., Sename, O., & Dugard, L. (2010). *Semi-active suspension control design for vehicles*, Elsevier.
- [4] Yu, M., Evangelou, S. A., & Dini D. (2023). *Advances in Active Suspension Systems for Road Vehicles*, *Engineering*, 33, 160-177, 2095-8099.
- [5] Sabu, T. (2021). *Overview of active suspension system in automobiles*, *International Research Journal of Engineering and Technology (IRJET)*, 8(7), 2395-0056.
- [6] Cytrynski, S., Neerpasch, U., Bellmann, R., & Danner, B. (2018). *The Active Suspension of the New Mercedes-Benz GLE*. *ATZ worldwide*, 120(12), 42-45.
- [7] Mercedes-Benz. (2024, March). *Funzionamento del Sistema E-ACTIVE BODY CONTROL*, In Mercedes-benz GLE Coupé Manuale marzo 2024 C167 MBUX. From: <https://www.mercedes-benz.it/passenger-cars/services/manuals.html/gle-coupe-2024-03-c167-mbox/e-abc/funzionamento-del-sistema-e-active-body-control?srsItd=AfmBOoq7cm4nkAZoSgr-u7wJlmsnr058hooBrF7VYa-Woh3wfb6gyLQuG>.
- [8] Tonoli, A., Amati, N., Galluzzi, R., Fornari, F. (2013). *Use of An Active Electro-Hydrostatic Actuation System for Vehicle Vibration Damping Applications*. (Intervento presentato al convegno 11th International Conference on Vibration Problems tenutosi a Lisbona, Portogallo nel 9-12 settembre 2013).

- [9] Galluzzi, R., Circosta, S., Amati, N., & Tonoli A. (2022). *Performance comparison between electromechanical and electro-hydrostatic regenerative shock absorbers*. In IOP Conference Series: Materials Science and Engineering (Vol. 1214, No. 1, p. 012012). IOP Publishing.
- [10] Liu, Y., Xu, L., & Zuo, L. (2017). *Design, modeling, lab, and field tests of a mechanical-motion-rectifier-based energy harvester using a ball-screw mechanism*. IEEE/ASME Transactions on mechatronics, 22(5), 1933-1943.
- [11] Li, Z., Zuo, L., Kuang, J., & Luhrs, G. (2012). *Energy-harvesting shock absorber with a mechanical motion rectifier*. Smart Materials and structures, 22(2), 025008.
- [12] Wellmann, T., Tousignant, T., Govindswamy, K., Tomazic, D., Steffens, C., & Janssen, P. (2019). *NVH Aspects of Electric Drive Unit Development and Vehicle Integration* (No. 2019-01-1454). SAE Technical Paper.
- [13] Young, S. (2014, July). *Vehicle NVH development process and technologies*. In Proceedings of the 21st International Congress, Beijing, China (pp. 13-17).
- [14] Vigé, D. (2010). *Vehicle interior noise refinement-cabin sound package design and development*. In Vehicle noise and vibration refinement (pp. 286-317). Woodhead Publishing.
- [15] Putra, A., Munir, F. A., & Juis, C. D. (2012). *On a simple technique to measure the airborne noise in a car interior using substitution source*. International Journal of Vehicle Noise and Vibration, 8(3), 275-287.
- [16] Cinkraut, J. (2015). *Transfer Path Analysis of a Passenger Car*.
- [17] Singh, A., Bharadwaj, S., & Narayan, S. (2016). *Analysis of various NVH sources of a combustion engine*. Tehnicki glasnik, 10(1-2), 29-37.
- [18] Kim, Y., Kim, C., Lee, J., & Kim, S. (2015). *Application of Experimental Transfer Path Analysis and Hybrid FRF-Based Substructuring Model to Structure-Borne Noise* (No. 2015-01-2267). SAE Technical Paper.

- [19] Toome, M. (2012). *Operational transfer path analysis: A study of source contribution predictions at low frequency*.
- [20] Cerrato, G. (2009). *Automotive sound quality-powertrain, road and wind noise*. *Sound and Vibration*, 43(4), 16-24.
- [21] Marano, D. (2021, May). *Progettazione acustica di trasmissioni meccaniche*. In *Organi di trasmissioni*.
- [22] Bisciaio, G. (2023). *Cycloidal drive design for Rotary Regenerative Shock Absorber* (Doctoral dissertation, Politecnico di Torino).
- [23] Dion, J. L., Pawelski, Z., Chianca, V., Zdziennicki, Z., Peyret, N., Uszpolewicz, G., ... & Lelasseux, X. (2020). *Theoretical and experimental study for an improved cycloid drive model*. *Journal of Applied Mechanics*, 87(1), 011002.
- [24] Vasic, M., Blagojevic, M., & Matejic, M. (2022). *Efficiency of non-pin wheel cycloid reducer concept*.
- [25] Tuma, J. (2014). *Vehicle gearbox noise and vibration: measurement, signal analysis, signal processing and noise reduction measures*. John Wiley & Sons.
- [26] Pascale, L., Marano, D., Langhart, J., Ebrahimi, S., Giese, T., & Eiselt, U. (2020, November). *Analisi e simulazione acustica di un assale elettrico*. In *Organi di trasmissioni*.
- [27] Asinari, P., Chiavazzo, E. (2020, March). *Selected Lectures on Engineering Thermodynamics* [PDF], Corso di Applicazioni avanzate di fisica tecnica, Politecnico di Torino.
- [28] Eisele, G., Wolff, K., Hoppermanns, J., & Genender, P. (2014). *15 Years of Transfer Path Analysis VINS in the Vehicle NVH Development-Selected Results (No. 2014-01-2047)*. SAE Technical Paper.

- [29] Eisele, G., Wolff, K., Alt, N., & Huser, M. (2005) *Application of vehicle interior noise simulation (VINS) for NVH analysis of a passenger car (No. 2005-01-2514)*. SAE Technical Paper.
- [30] Panda, K. C. (2016). *Dealing with noise and vibration in automotive industry*. *Procedia Engineering*, 144, 1167-1174.
- [31] AVL. *AVL EXCITE™ Acoustic User Manual*, In AVL Resource Box.